The FtsLB subcomplex of the bacterial divisome is a tetramer with an uninterrupted FtsL helix linking the transmembrane and periplasmic regions

Received for publication, October 15, 2017, and in revised form, December 4, 2017 Published, Papers in Press, December 12, 2017, DOI 10.1074/jbc.RA117.000426

Samson G. F. Condon[‡§1,2,3], Deena-Al Mahbuba[‡§1,4], Claire R. Armstrong[‡], Gladys Diaz-Vazquez[‡¶2,5], Samuel J. Craven[‡§6], Loren M. LaPointe[‡§], Ambalika S. Khadria[‡§], Rahul Chadda[‖7], John A. Crooks[‡§8], Nambirajan Rangarajan[‡], Douglas B. Weibel[‡8], Aaron A. Hoskins[‡9], Janice L. Robertson[‖7], Qiang Cui[**], and Alessandro Senes[‡10]

From the [‡]Department of Biochemistry, the [§]Integrated Program in Biochemistry, the [¶]Biophysics Graduate Program, and the [**]Department of Chemistry, University of Wisconsin, Madison, Wisconsin 53706 and the [‖]Department of Molecular Physiology and Biophysics, University of Iowa Carver College of Medicine, Iowa City, Iowa 52242

Edited by Karen G. Fleming

In *Escherichia coli*, FtsLB plays a central role in the initiation of cell division, possibly transducing a signal that will eventually lead to the activation of peptidoglycan remodeling at the forming septum. The molecular mechanisms by which FtsLB operates in the divisome, however, are not understood. Here, we present a structural analysis of the FtsLB complex, performed with biophysical, computational, and *in vivo* methods, that establishes the organization of the transmembrane region and proximal coiled coil of the complex. FRET analysis *in vitro* is consistent with formation of a tetramer composed of two FtsL and two FtsB subunits. We predicted subunit contacts through co-evolutionary analysis and used them to compute a structural model of the complex. The transmembrane region of FtsLB is stabilized by hydrophobic packing and by a complex network of hydrogen bonds. The coiled coil domain probably terminates near the critical constriction control domain, which might correspond to a structural transition. The presence of strongly polar amino acids within the core of the tetrameric coiled coil suggests that the coil may split into two independent FtsQ-binding domains. The helix of FtsB is interrupted between the transmembrane and coiled coil regions by a flexible Gly-rich linker. Conversely, the data suggest that FtsL forms an uninterrupted helix across the two regions and that the integrity of this helix is indispensable for the function of the complex. The FtsL helix is thus a candidate for acting as a potential mechanical connection to communicate conformational changes between periplasmic, membrane, and cytoplasmic regions.

The cell envelope of Gram-negative bacteria, such as *Escherichia coli*, consists of three layers: a cytoplasmic membrane, an outer membrane, and a rigid cell wall formed by a mesh of peptidoglycan located in the intervening periplasmic space. Cell division requires mechanisms for the separation of these three layers. The first step is the establishment of a division site and the segregation of the duplicated chromosome. This allows for the beginning of constriction, during which the coordinated activities of numerous peptidoglycan synthases and hydrolases remodel the cell wall. Finally, the process leads to membrane fusion and to the separation of two daughter cells. The large multiprotein complex that supports a majority of these functions is called the divisome.

At least 3 dozen proteins are known to participate in cell division in *E. coli*, but the essential components of the divisome consist of a core of 12 proteins. Their recruitment to mid-cell follows a hierarchical order of dependence (FtsZ → FtsA-ZipA → FtsE-FtsX → FtsK → FtsQ → FtsL-FtsB → FtsW → FtsI → FtsN; Fig. 1*a*), which also reflects, in part, the timing and interactions that occur in the complex assembly (1–12). The divisome assembles around the tubulin homolog FtsZ, which forms a ringlike structure at mid-cell (the Z-ring) (13–15). FtsZ protofilaments treadmill around the circumference of the cell, providing a scaffold for the recruitment and movement of the components around the cell and ultimately leading to incorporation of new peptidoglycan around the forming septum (16, 17). FtsZ is tethered to the plasma membrane by the cooperative action of ZipA, a single-pass transmembrane (TM)[11] protein (18, 19), and of FtsA, an actin homolog and peripheral membrane protein able to form protofilaments (20). Other early components

This work was supported in part by National Institutes of Health (NIH) Grant R01-GM099752, National Science Foundation (NSF) Grant CHE-1415910 (to A. S.), and NSF Grant DMS-1661900 (to Q. C.). The authors declare that they have no conflicts of interest with the contents of this article. The content is solely the responsibility of the authors and does not necessarily represent the official views of the National Institutes of Health.

This article contains Table S1 and Figs. S1–S9.

[1] Both authors contributed equally to this work.

[2] Supported by National Library of Medicine (NLM) Training Grant 5T15LM007359 to the Computation and Informatics in Biology and Medicine (CIBM) Training Program.
[3] Supported by a William R. and Dorothy E. Sullivan Wisconsin Distinguished Graduate Fellowship.
[4] Supported by the Steenbock Predoctoral Fellowship.
[5] Supported by a Science and Medicine Graduate Research Scholars (SciMed GRS) fellowship.
[6] Supported by the Dr. James Chieh-Hsia Mao Wisconsin Distinguished Graduate Fellowship and by the William H. Peterson Fellowship.
[7] Supported by NIH Grant R01-GM120260.
[8] Supported by NSF Grant DMR-1121288.
[9] Supported by a Shaw Scientist Award, a Beckman Young Investigator Award, and startup funds from the University of Wisconsin (Madison, WI).

[10] To whom correspondence should be addressed. E-mail: senes@wisc.edu.

[11] The abbreviations used are: TM, transmembrane; MSL, Molecular Software Library; bEBL, backbone-dependent energy-based conformer library; RMSD, root mean square deviation; DM, *n*-decyl-β-D-maltopyranoside; DDM, *n*-dodecyl-β-D-maltoside; MD, molecular dynamics; CCD, constriction control domain; Ni-NTA, nickel-nitrilotriacetic acid; LB, Luria broth; Cy3 and Cy5, Cyanine 3 and 5, respectively; TCEP, tris(2-carboxyethyl)phosphine; BisTris, 2-[bis(2-hydroxyethyl)amino]-2-(hydroxymethyl)propane-1,3-diol.

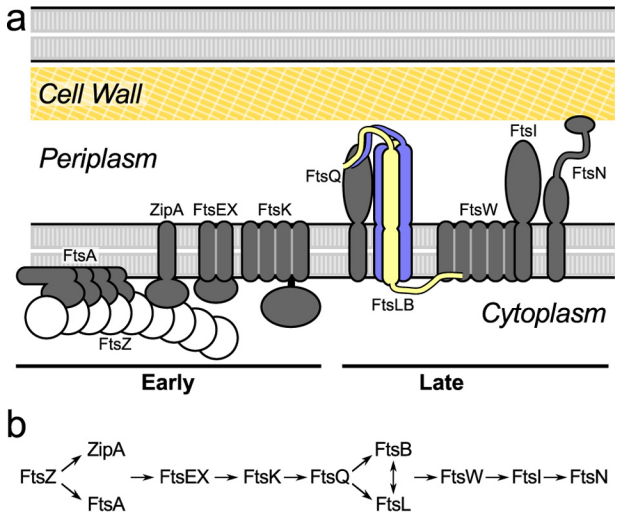

Figure 1. The essential proteins of the divisome. *a*, schematic representation of the divisome of *E. coli*. The complex assembles around a polymeric scaffold formed by FtsZ. With a few exceptions (FtsZ, FtsA, and FtsE), all essential components are integral membrane proteins. As reported in this work, the FtsLB complex is a heterotetramer formed by two FtsL subunits (*yellow*) and two FtsB subunits (*blue*). The complex forms an extended helical bundle that comprises the transmembrane helices and the periplasmic coiled coil. The C-terminal periplasmic tails of FtsLB mediate the binding to FtsQ. The cytoplasmic tail of FtsL has been hypothesized to bind to FtsW. Description of the function of the various components is provided in the Introduction. *b*, the divisome of *E. coli* displays a characteristic hierarchy of recruitment at the division site, with the *arrows* indicating a dependence of a component on the one that precedes it in the sequence. The hierarchy also roughly corresponds to the order of recruitment, which can be subdivided into early and late components.

of the divisome include FtsEX, an ABC transporter-like complex that controls cell wall hydrolysis and possibly divisome assembly (21, 22), as well as FtsK, a DNA translocase important for chromosome segregation (23).

The late components of the divisome (FtsQ, FtsB, FtsL, FtsW, FtsI, and FtsN) localize approximately at the beginning of constriction (24). FtsQ, FtsB, and FtsL are three bitopic (single-pass) membrane proteins that form a complex whose exact function is not well understood (6). The FtsQLB complex is required for the recruitment of FtsW, a large multispan membrane protein, and FtsI, a bitopic protein. FtsW and FtsI work in coordination to synthesize septal cell wall (8); FtsI is a penicillin-binding protein (PBP3) with transpeptidase activity (25), and FtsW is most likely its cognate glycosyltransferase (26–28) (FtsW has also been proposed to be a flippase for peptidoglycan precursors (29, 30)). The last protein in the recruitment hierarchy is FtsN, a bitopic protein with an N-terminal TM domain, a predicted disordered region, and a C-terminal domain capable of recognizing septal peptidoglycan (31). The precise role of FtsN is not understood, but its accumulation at the septal ring represents a key event for triggering constriction. This activation may be mediated by some of the interactions that have been postulated for FtsN, which include FtsA, the peptidoglycan synthase complex (FtsW, FtsI, and PBP1B), and the FtsQLB complex (32–36).

Because the divisome consists primarily of integral membrane proteins, its structural characterization has been lagging and limited to fragments of water-soluble domains (31, 37–40). Here we focus on the structural organization of the FtsL-FtsB subcomplex (FtsLB), which has been implicated as a critical player in triggering constriction (41, 42). Topologically, FtsL and FtsB are both small bitopic proteins with a nearly identical domain organization, which suggests that they may derive from a common evolutionary ancestor. Both proteins have short (or absent) N-terminal cytoplasmic tails, one TM domain, a juxtamembrane coiled coil, and C-terminal tails in the periplasm (Fig. 1*a*). Peptides corresponding to the TM helices form a stable higher-order oligomer *in vitro*, with an equal number of FtsL and FtsB subunits, indicating that the TM region is an important contributor to the stability of the complex (43). This is consistent with the observation that the TM domains are biologically important (6, 44, 45). FtsL and FtsB associate *in vivo* even in the absence of FtsQ (11, 46), although FtsQ is required for their recruitment to mid-cell (6). The association with FtsQ to form the FtsQLB complex is primarily mediated by the C-terminal tails of FtsLB, which bind to the C-terminal end of FtsQ, as evidenced by truncation functional analysis (45, 47) as well as cross-linking performed *in vivo* (48). The periplasmic domains of the three proteins are sufficient to form soluble complexes with submicromolar binding affinities, as established for *E. coli* (49) and *Streptococcus pneumoniae* (50, 51) proteins. Notably, these studies have been performed using solubilized FtsLB constructs that were fused to a stable heterodimeric coiled coil and thus forced into a dimeric state. However, FtsLB is likely to be a higher-order oligomer (such as a tetramer), as evidenced by biophysical analysis of their TM helices in isolation (43). The tight binding affinity of these 1:1:1 FtsQLB soluble constructs therefore suggests that independent FtsQ-binding sites exist in FtsLB, each formed by one FtsL and one FtsB subunit.

The precise function of FtsLB has not yet been determined. It was originally hypothesized that FtsLB could have a structural role in stabilizing the divisome (45, 47). The finding that FtsL is subject to active degradation unless it is stabilized by interaction with FtsB in *Bacillus subtilis* (52–54) and *E. coli* (45) suggested that FtsL levels may be rate-limiting for division (54). More recent evidence indicates that FtsLB is an active participant in the decision making that controls the cell division process, playing a central role in triggering of septal peptidoglycan synthesis. This hypothesis is supported by observations that point mutations in a particular region of FtsL and FtsB alter the tightly regulated cell division process, allowing it to proceed even in situations in which normally it would not occur (41, 42). Tsang and Bernhardt (41) discovered that a single point mutation in FtsL (E88K) allows the cells to bypass the normally strict requirements for other division proteins, namely FtsK, ZipA, FtsN, and FtsA (although residual levels of FtsA expression appear to be still necessary). Independently, De Boer and colleagues (42) identified a series of mutants that bypass the need for FtsN. These mutants map to two short regions of the coiled coil of FtsL (residues 88–94) and FtsB (residues 55–59). These regions, which are located ~30 residues past the TM domain, were named the "constriction control domain" (CCD) (42).

The observed properties of these CCD mutants are consistent with a conformational change in FtsLB that has become deregulated. In other words, an OFF/ON structural transition in FtsLB may be part of the events that control the beginning of

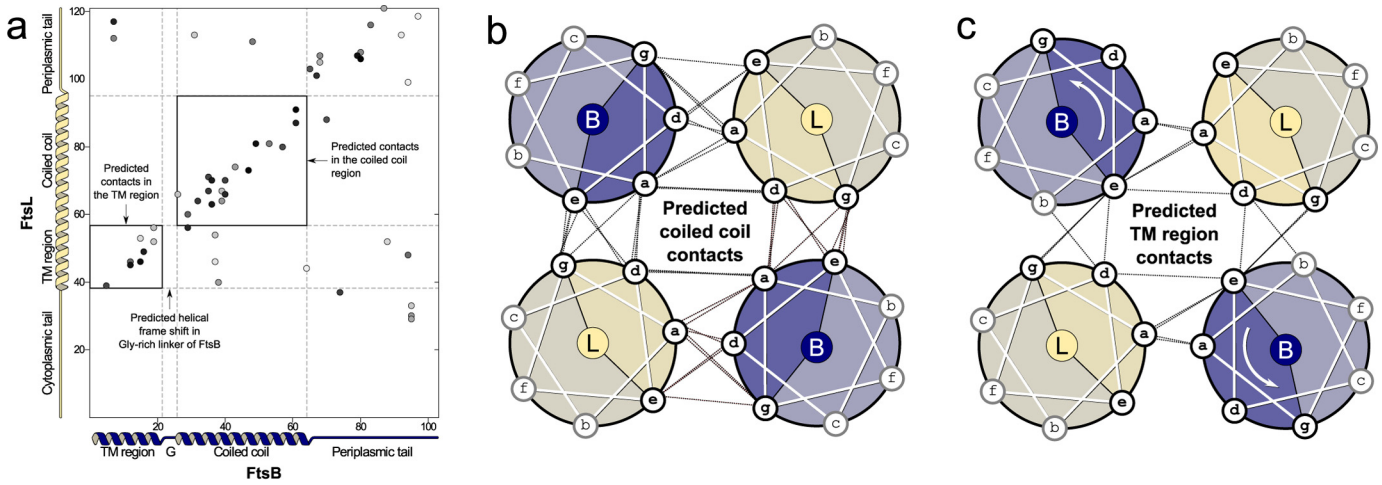

Figure 2. Co-evolutionary analysis identifies a self-consistent map of contacts in the FtsLB helical bundle. *a*, map of potential contacts between positions in the sequence in FtsB (*x* axis) and FtsL (*y* axis), inferred by co-evolutionary analysis. Displayed are the top 95 pairs identified by the analysis (the *darkness* of the *shading* reflects their ranking). The complete ranked list is provided in Table S1. The TM region and coiled coil are *highlighted* by *boxes*. *Marked* in the sequence of FtsB is also the position of a Gly-rich region between the TM and coil domains (*G*). *b*, predicted contacts in the coiled coil domain between FtsB (*blue*) and FtsL (*yellow*) displayed using a helical-wheel projection. The contacts are in excellent agreement with the expected contacts for a canonical coiled coil. *c*, similar map for the TM region. The contacts are also consistent with the formation of a helical bundle. The interfacial positions of FtsL are on the same face of the interfacial position in the coiled coil, suggesting that FtsL forms a continuous helix. The positions in FtsB are rotated by ~60° with respect to those of the coiled coil (*white arrow*), indicating that a discontinuity is probably present between the two helical domains.

cell constriction. This transition may be triggered allosterically by FtsN itself, as suggested by the observation that the essential region of FtsN (^{E}FtsN, a short stretch of sequence that is separated by ~20 amino acids from the C-terminal side of the TM domain) is in a position that is topologically equivalent with the location of the CCD in FtsLB (41, 42).

To elucidate the effect of the CCD mutants and the overall function of the FtsQLB complex in molecular detail, it is necessary to understand its structural organization. So far, two partial structures have been obtained. The structure of the periplasmic domain of FtsQ has been solved by X-ray crystallography, without the TM and cytoplasmic domains (39). Additionally, we previously determined the crystal structure of the coiled coil domain of FtsB and also produced a computational model of the TM domain of the same protein, based on mutagenesis data (38). Both structures were obtained in the absence of FtsL and in a homodimeric form. In addition, computational models of the FtsQLB periplasmic region (both in the trimeric and hexameric state) have also been reported (55). These models were based on available experimental data regarding contacts between FtsQ and FtsLB, whereas the FtsLB component was predicted *ab initio*. Additionally, these models lacked the TM region.

Here, we present a structural analysis of the TM domain and periplasmic coiled coil of FtsLB, based on a combination of biophysical and computational methods with *in vivo* validation. The work includes *in vitro* FRET to determine the oligomerization state of FtsLB; a co-evolutionary analysis of sequence alignments to provide an extensive set of predicted contacts between positions in FtsL and FtsB; molecular modeling to compute a three-dimensional structural model of the complex; molecular dynamics in lipid bilayers to evaluate stability and dynamics of the model; and a functional analysis of mutants *in vivo* to experimentally test the model and investigate the biological relevance of the predicted structural features.

Our results confirm that FtsLB is a higher oligomer and point to an L_2B_2 tetramer. Overall, the phenotypic analysis is in good agreement with structural features identified computationally. The distribution of deleterious phenotypes among the TM region mutants is consistent with the predicted interface. We confirm that the helix of FtsB breaks between the TM and periplasmic regions, with the formation of a flexible linker, as hypothesized previously (38). In contrast, we show that FtsL forms a continuous helix and that the integrity of this helix is crucial for function. We also found indications that the coiled coil might not be built for structural stability, at least not in the form of a canonical tetrameric helical bundle assembly, suggesting that the coil may either serve as a dynamic structural unit or else split into two independent domains.

Results and discussion

Co-evolutionary analysis identifies potential quaternary contacts consistent with an extended helical bundle

To predict the positions that mediate the association of the FtsLB complex, we analyzed a paired alignment of FtsL and FtsB sequences from proteobacteria species using the EV-Couplings algorithm (56). EV-Couplings uses a maximum-entropy model of the evolutionary history of a protein (or protein complex) to infer potential tertiary (56) and quaternary (57) contacts in its structure. It is based on the notion that, to maintain complementary interactions, amino acid changes influence the variation of positions that are in close proximity. The results of our EV-Couplings analysis are shown in Fig. 2*a*. The figure displays the top 95 pairs of positions identified between FtsL and FtsB. The complete ranked list is provided in Table S1. FtsB-FtsB and FtsL-FtsL pairs are displayed in Fig. S1.

A notable diagonal pattern of co-evolving positions starts in the TM region of both proteins and continues in the coiled coil

region, which is consistent with the contact map expected for an extended parallel helical bundle. As shown in the helical wheel diagram of Fig. 2*b*, the co-evolving positions in the periplasmic region are also consistent with the expected geometry of a coiled coil (7, 50, 58), occurring at positions of the "heptad repeat" (*abcdefg*) that are interfacial, at either the buried *a* and *d* positions or at the partially solvent exposed *e* and *g* positions. Moreover, these predicted contacts occur between pairs that are in proximity in a canonical coiled coil (*e.g. a-a*, *a-d*, and *g-e*, but not *a-e*). The pattern of connectivity remains in good agreement with a coiled coil contact map until positions 61 in FtsB and 91 in FtsL, after which it loses this periodicity. This range covers approximately five heptad repeats, which for FtsB is ~10–20 amino acids shorter than the consensus of the sequence-based predictors Paircoil (59), Multicoil (60), Marcoil (61), and Coils (62, 63) (inferring the length of the coiled coil of FtsL with the same methods is difficult because it is poorly predicted (58)). The coiled coil predicted by the evolutionary analysis approximately reaches the CCD (55–59 in FtsB, 88–94 in FtsL, *highlighted* in *yellow* in Fig. 2, *a* and *d*), suggesting that it is possible that this critical regulatory region occurs toward the end of the coil and thus in proximity of a structural transition.

A continuous FtsL helix and a discontinuous FtsB

As illustrated in the helical wheel diagram of Fig. 2*c*, the TM region also displays a pattern of predicted contacts consistent with a bundle of parallel helices. The co-evolving positions are clustered toward the C-terminal side of the TM domains. Remarkably, the interfacial positions of the TM domain FtsB are in excellent agreement with those identified previously from their sensitivity to mutagenesis in a self-association assay (38).

Comparison of the contact maps (Fig. 2, *b* and *c*) indicates that, in FtsL, the predicted interfaces of coiled coil and TM domains occur on the same face of the helix (involving the *a*, *d*, and *g* positions in the TM domain and the *a*, *d*, *e*, and *g* positions in the coil). This pattern indicates that FtsL forms a continuous helix across the membrane and the periplasmic region. A different outcome is observed for FtsB, for which the TM domain interface involves *a* and *e* but also *b* positions (*versus a*, *d*, *e*, and *g* positions in the coil) and thus appears rotated by ~60° with respect to the periplasmic region (as indicated by the *arrow* in Fig. 2*c*). This rotation suggests the presence of a helical break. Rearrangements of the periodicity from the canonical heptad repeat are not uncommon in long coils. The 60° shift of the relative orientation of the interface between the TM and coiled coil regions of FtsB would correspond to the insertion of four amino acids (*abcdabcdefg*), which is designated as a "stutter" (64, 65). Such mismatches influence the coil's local structure and can possibly facilitate conformational changes necessary for function (66, 67). In this particular case, however, the presence of a conserved Gly-rich region (^{22}GKNG^{25} in *E. coli* and ^{22}GKGG^{25} in the consensus sequence of α-, β-, and γ-proteobacteria (38)) suggests that the juxtamembrane linker of FtsB is more likely to adopt a flexible and extended conformation instead of a local distortion of the helix.

FtsLB is a higher oligomer, probably an L_2B_2 tetrameric complex

To build a structural model for the FtsLB complex based on the evolutionary constraints, it was necessary to establish its oligomeric state. In previous work, we demonstrated that the isolated TM region of the FtsLB complex assembles to form a higher-order oligomer consisting of an equal number of FtsL and FtsB subunits, but we were unable to distinguish between heterotetrameric (L_2B_2), heterohexameric (L_3B_3), or even higher oligomeric forms (43). Here, we assessed the stoichiometry of a construct that includes both periplasmic and TM domains by FRET analysis *in vitro*.

The FtsLB complex was overexpressed in *E. coli*, consisting of an N-terminally His-tagged FtsB and an N-terminally Strep-tagged FtsL. FtsL and FtsB were co-expressed. The proteins co-purify over sequential Ni-NTA and streptavidin columns in DM and DDM detergents, indicating that they form a stable complex with a density over Coomassie staining compatible with a 1:1 stoichiometric ratio (Fig. S2*a*). A C-terminal Cys residue was introduced in either FtsB or FtsL, and protein samples were separately labeled with either donor (Cyanine 3; Cy3) or acceptor (Cyanine 5; Cy5) fluorophores. Because the stoichiometric analysis is performed separately for the two proteins, to further confirm interaction between FtsL and FtsB in the experimental conditions, we mixed and equilibrated $FtsL_{unlabeled}$-$FtsB_{Cy3}$ and $FtsL_{Cy5}$-$FtsB_{unlabeled}$ samples, which produced a distinct FRET signal (Fig. S2*b*).

We analyzed the stoichiometry of FtsLB by adopting a FRET method based on changing the relative fraction of donor- and acceptor-labeled molecules while the total protein concentration was maintained constant (68). In these conditions, the theoretical variation of donor quenching (Q) depends on the oligomeric state of the complex, being proportional to $(1 - P_D^{n-1})$, where P_D is the relative fraction of donor-labeled protein, and n is the number of subunits in the complex (see Equation 4 under "Experimental procedures"). Due to the power law, no variation of donor quenching is expected for monomers as the donor fraction decreases, a linear increase of Q is expected for dimers, and a curved relationship is expected for trimers and higher oligomers. We performed two independent experiments, labeling only one of the two proteins with donor and acceptor fluorophores while leaving the other unlabeled. By labeling only either the FtsL or the FtsB moieties of the FtsLB complex, the procedure allowed us to calculate the number of subunits of FtsL and of FtsB individually.

As illustrated in Fig. 3 (*left*), donor quenching increased linearly for FtsL-labeled samples when the acceptor fraction was increased. We used the sum of residuals between the experimental data and the models to compare the fits. The residual of the two-subunit linear model (*dashed line*, residual (r) = 0.001) is 10-fold smaller than the residuals of the three-subunit model (*continuous line*, r = 0.01), indicating that two FtsL molecules are present in the FtsLB complex. The quenching data of FtsB (Fig. 3, *right*) also display a progressive increase of donor quenching, establishing that at least two FtsB subunits are present in the FtsLB complex. However, the fit to two subunits (r = 0.0055) is only marginally better than the fit to three subunits

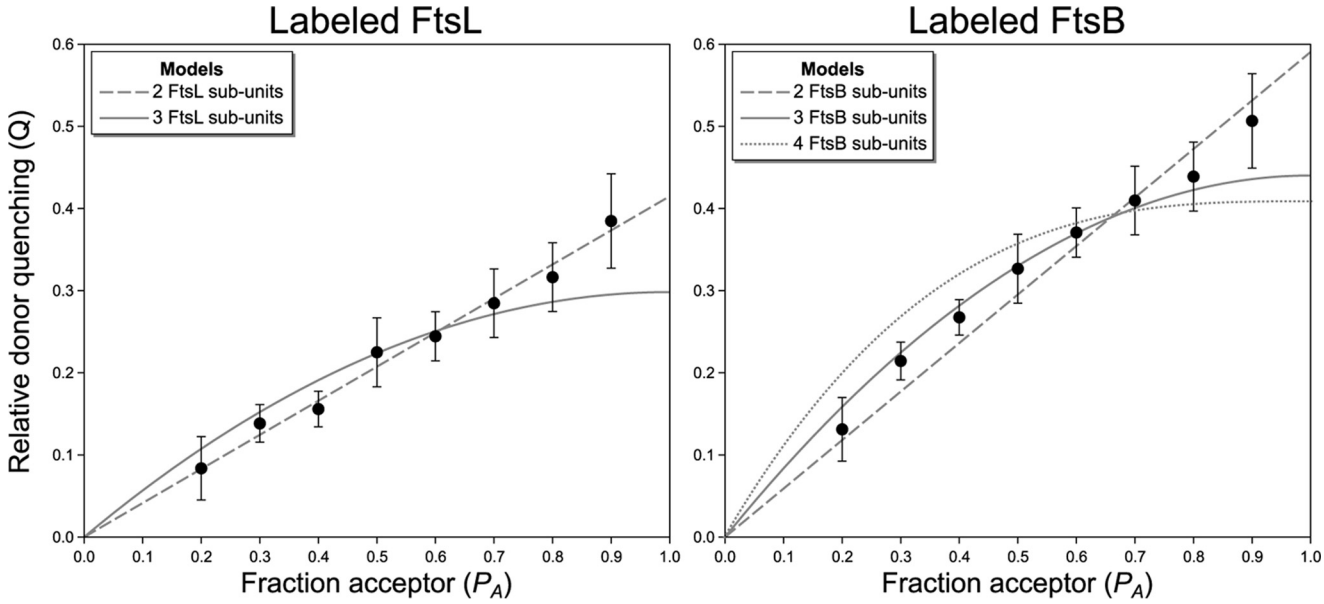

Figure 3. FRET analysis indicates FtsLB is a 2:2 tetramer. Analysis of the stoichiometry of Cy3- and Cy5-labeled FtsLB complexes was performed in DDM detergent. Two independent analyses were performed to count the subunits of FtsL (*left*) and FtsB (*right*) by labeling only one of the two proteins of the complex. *Left*, the FRET data of FtsL fit well to a two-subunit stoichiometry (*dashed line*, sum of residuals $r = 0.0010$) with respect to a three-subunit model (*continuous line*, $r = 0.0111$). *Right*, the fit for FtsB establishes that there are at least two subunits but does not differentiate between two- and three-subunit models ($r = 0.0055$ and 0.0064, respectively). A four-subunit model can be excluded (*dotted line*, $r = 0.0224$). Considering prior evidence and likely symmetry, the most likely model for FtsLB is a 2:2 heterotetramer.

($r = 0.0064$); therefore, the data cannot differentiate between these two models, as in the case of FtsL. The fit, however, can reasonably rule out a four-subunit model (*dotted line*, $r = 0.02$).

Overall, the analysis confirms that the FtsLB complex is a higher-order oligomer. Considering the entire body of available evidence, the most likely model is an L_2B_2 heterotetramer. Because FtsL fits well to a model containing two subunits, the possible states supported by the data are L_2B_2 or L_2B_3 stoichiometries. However, a 2:3 stoichiometry is in disagreement with previous FRET data that indicated that the FtsLB complex has an equivalent number of FtsL and FtsB subunits (43). A 2:3 pentamer is also a less common oligomeric form in nature than a 2:2 heterotetramer (69). In addition, a 2:3 pentamer would be necessarily asymmetrical, whereas the co-evolutionary contacts are strongly consistent with a standard symmetrical organization (Fig. 2, *b* and *c*). Finally, 2:2 would also be consistent with a previous estimate of the stoichiometry of the divisome based on ribosome profiling data (70).

Molecular modeling of the FtsLB helical bundle

We used a Monte Carlo docking procedure guided by the evolutionarily based distance constraints to create an all-atom computational model of the structure of the TM and coiled coil domains of the tetrameric complex (residues 1–61 of FtsB and 35–91 of FtsL). The model, which is illustrated in Fig. 4*a*, consists of a four-helix bundle that spans the membrane and projects into the periplasmic region for ~55 Å. The structure is well packed, with the exception of a small void (~12 $Å^3$) present at the level of the juxtamembrane linker region. A majority of the co-evolutionary distance constraints used to derive the model (*dashed lines* in the figure, listed in Table S1) are satisfied; of the 27 side chain pairs involved, 22 are in contact (minimal distance between heavy atoms (d_{min}) < 5 Å), four are in proximity (d_{min} < 10 Å), and only one pair is separated by over 10 Å (FtsL Gln-66 with FtsB Ile-26). Because an L_3B_3 hexamer could not be entirely excluded, we also modeled this stoichiometry. The co-evolutionary restraints were well satisfied by the resulting model, but the model is significantly underpacked, with the presence of an incomplete pore spanning parts of the TM and coiled coil domains (Fig. S3). For this reason, the L_3B_3 model was no longer pursued.

The TM region of the L_2B_2 model forms a helical bundle characterized by a left-handed crossing angle (7° for FtsB and 10° for FtsL, tilt angle of the helices with respect to the membrane normal). The two TM helices of FtsB are in closer proximity to each other compared with the two helices of FtsL (interhelical distance of 13.6 and 15.2 Å, respectively). Remarkably, the conformation of FtsB is similar to a model of a FtsB dimer that we obtained previously (RMSD of 2.5 Å; Fig. S4). This previous model was obtained from the effect of point mutations on the homodimerization of the TM domain of FtsB in the absence of FtsL, as assayed with TOXCAT (38). The convergence of two completely independent sets of data, evolutionary information and experimental mutagenesis, to a similar model is a strong indication that the conformation and interface of the TM helices of FtsB are correctly predicted.

The C-terminal side of the TM region contains a number of side chains that can form hydrogen bonds, including the polar Gln-16. In the lowest-energy model, Gln-16 acts as a hydrogen bond donor to the side chain hydroxyl group of Thr-49 of FtsL (Fig. 4*b*). Small changes in conformation would allow alternative interactions of Gln-16 with a number of other donor and acceptor groups. In particular, Gln-16 could form self-interactions with Gln-16 from the opposing chain as well as potential hydrogen bonds with Thr-52 of FtsL and Trp-20 of FtsB.

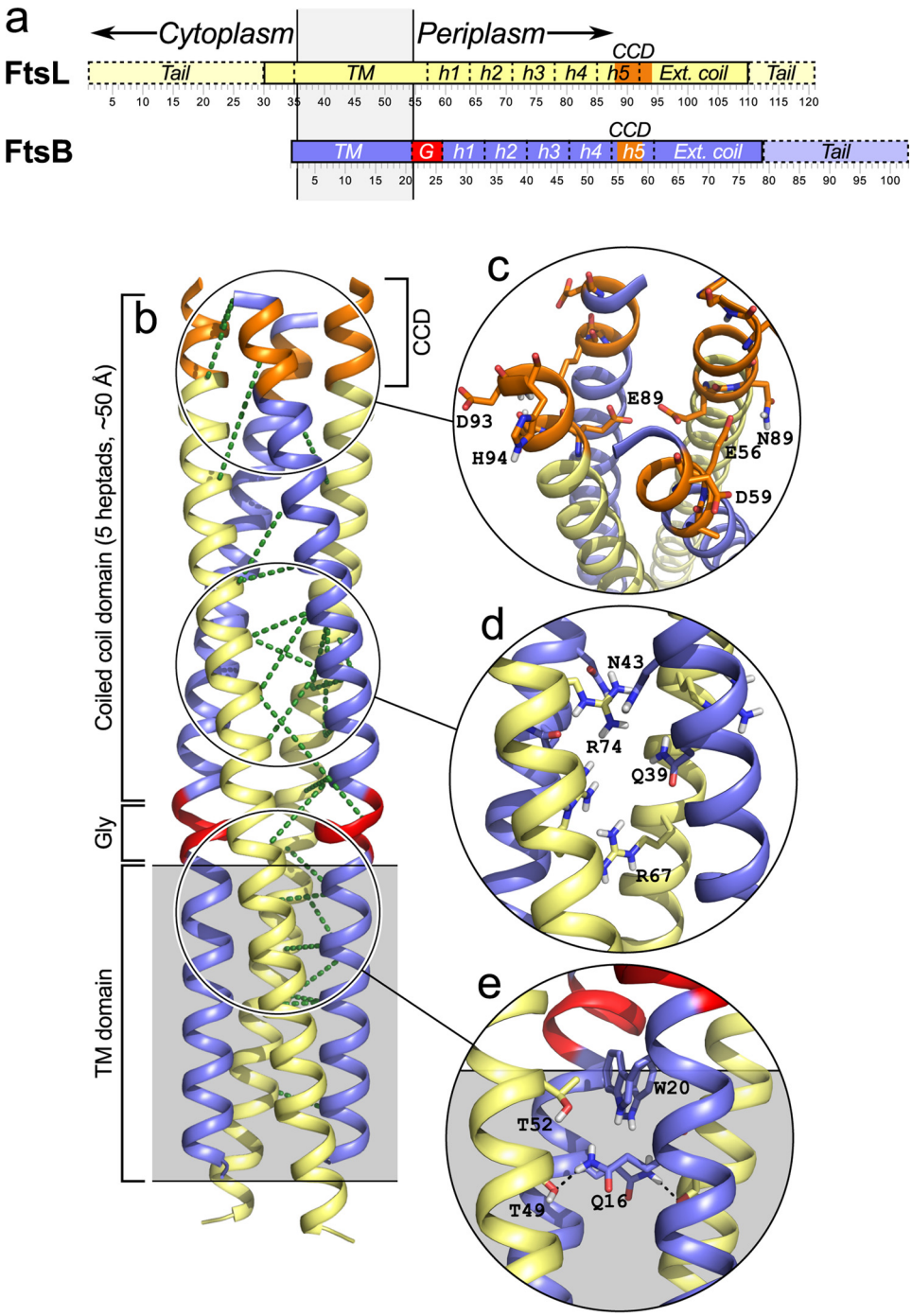

Figure 4. Computational model of FtsLB: A bundle with a helical break in FtsB. *a*, schematic representation of the domains of FtsL and FtsB as discussed in this work. The five heptad repeats in the coiled coil are designated as *h1*, *h2*, etc. *Ext. coil*, extended coil region, as defined for the MD analysis. *G* (*red*), Gly-rich linker in FtsB. The tails that are absent in the modeling are represented with *dashed lines*. The position of the CCD region is *marked* in *orange*. *b*, *ribbon representation* of the model of the FtsLB complex. The *dashed lines* represent the co-evolutionary constraints applied to obtain the model. FtsL (*yellow*) consists of continuous helices that traverse the membrane into the periplasmic region. The helix of FtsB (*blue*) is modeled in an unwound conformation in the juxtamembrane Gly-rich region (*red*). *c*, detail of the CCD region. If the coiled coil conformation persists beyond this region, the polar side chain of Glu-88 would be buried in the coil's core. *d*, the lower coiled coil also contains a cluster of very polar amino acids buried in the core (Gln-39 and Asn-41 from FtsB; Arg-67 and Arg-74 from FtsL). These amino acids are likely to be destabilizing if buried in a canonical coiled coil, as represented by the model. *e*, the TM region contains a cluster of amino acids able to form hydrogen bonds (Gln-16, Tyr-17, and Trp-20 from FtsB; Thr-49, Thr-52, and Thr-56 from FtsL), which may contribute to stabilize this domain.

As expected, FtsL was modeled as a continuous helix across the TM and coiled coil domains. Also as expected, the change of orientation of the interface between the same two domains of FtsB required the introduction of a break in the α-helix in the juxtamembrane region (*red* in Fig. 4). We opted to model the linker in the least perturbing conformation (an unwound helix), although the Gly-rich linker is likely to adopt a more extended conformation. The relative flexibility of the linker regions of FtsL and FtsB will be addressed later using molecular dynamics.

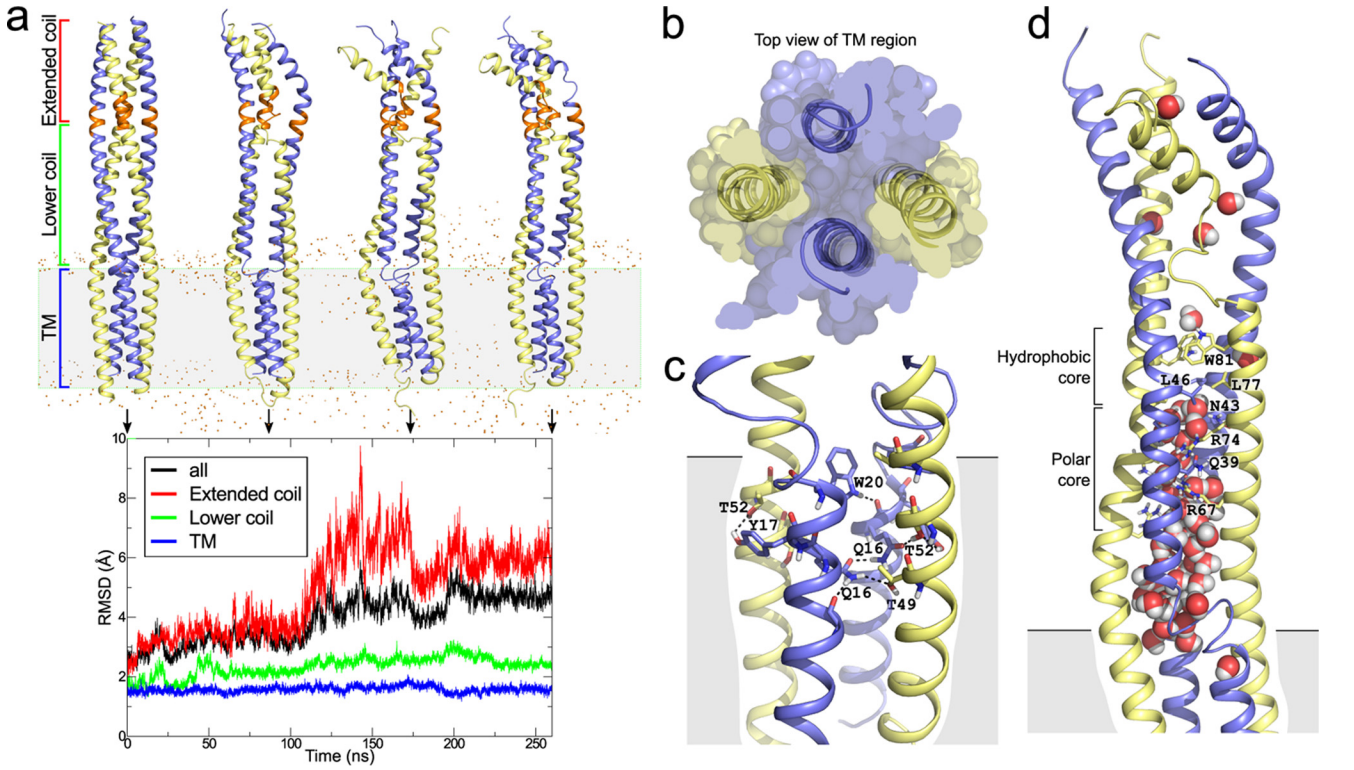

Figure 5. A stable TM region, a dynamic coiled coil. *a*, trajectory of the 260-ns run, with displayed conformations at 0, 87, 173, and 260 ns. The RMSD analysis is shown for the entire complex (*black*), the TM region (*blue*), the lower coil (*green*; 29–61 of FtsB and 57–91 of FtsL), and the extended coil (*red*, 62–79 of FtsB and 92–110 of FtsL). The CCD, which separates the lower from the extended coil, is in *orange*. As evident from the RMSD traces, the TM and lower coil are stable during the simulation, whereas the upper coil diverges, although it retains some helicity and interaction between pairs of FtsL and FtsB chains. The unfolding of the Gly-rich linker in the juxtamembrane region of FtsB is also evident. *b*, the TM region seen from above the membrane; the region rearranges during the simulation to bring the two FtsB helices (*blue*) closer to each other and in contact, whereas the FtsL helices are now separated from each other. *c*, a configuration of the extended hydrogen bonding network present in the C-terminal side of the TM region, involving Gln-16, Tyr-17, and Trp-20 of FtsB and three threonine residues (Thr-49, -52, and -56) of FtsL. *d*, a view of the water that invades the core of the lower coiled coil, hydrating otherwise buried side chains or Arg-67, Arg-74, Gln-39, and Asn-43.

The periplasmic region (residues 27–61 in FtsB and 58–91 in FtsL) produced a well-packed canonical coiled coil. The coil is approximately five heptad repeats long (~35 amino acids). Interestingly, the domain is unusually rich in polar amino acids occurring at *a* and *d* buried positions, with a total of 12. These polar amino acids are equally contributed by both proteins (three per subunit), although FtsB contains only neutral side chains (Gln-39, Asn-43, and Asn-50), whereas FtsL contains amino acids that are normally charged (Arg-67, Arg-74, and Glu-80). A region around the second and third heptad repeats of the coiled coil is particularly polar, where Arg-67 and Arg-74 from FtsL and Gln-39 and Asn-43 from FtsB occur in close proximity. The presence of so many buried hydrophilic side chains is interesting because they are likely to destabilize the coiled coil. In particular, the four Arg residues contributed by FtsL would be charged even if buried inside the protein core and thus very costly to desolvate (71). Another potentially charged side chain, Glu-80 in FtsL, is in the core in the modeled complex, but it is placed toward the end of the predicted coiled coil, near the CCD region, and thus it may be solvent-accessible.

Molecular dynamics suggest a stable TM region with an intricate network of hydrogen bonding

Two features, the presence of a flexible linker and a potentially destabilized coiled coil, raise questions about the dynamic properties of the FtsLB complex. To address them, we performed molecular dynamics (MD) simulations of the FtsLB model in explicit POPE bilayers. For this simulation, we extended the coiled coil conformation by ~20 amino acids beyond the region predicted by the co-evolutionary contacts, to avoid end effects and to test the coil boundaries. We will refer to this added region as the "extended coil" (residues 92–110 for FtsL and 62–79 for FtsB) and to the section predicted by the co-evolutionary analysis as the "lower coil" (residues 29–61 of FtsB and 57–91 of FtsL). Three replica MD simulations were run for 260 ns (run 1; Fig. 5) and for 200 ns (runs 2 and 3; Fig. S5).

During the simulation, the RMSD from the initial structure increases to ~4, 5, and 6 Å in the three replica runs (*black traces* in Fig. 5*a* and Fig. S5). The majority of these changes are localized to the "extended coil" section (*red traces*), which quickly separates and partially unfolds. The lower coil remains relatively stable during the run (final RMSD around 2.3, 3.4, and 2.9 Å; *green traces*). The most stable region is the TM domain, which remains stable for the entire run across all three simulations, with average RMSDs around 1.6, 1.9, and 2.3 Å during the three runs (*blue traces*).

A slight rearrangement of the relative orientation of the TM helices is observed, which brings the two FtsB helices closer to each other by ~1–2 Å and, consequently, further separates the FtsL helices by a similar distance. This rearrangement gives the

bundle a less "square" and more "rhomboid" configuration, one in which extensive packing occurs not only between FtsL and FtsB but also between the two FtsB helices, whereas the contacts between the two FtsL helices become reduced (Fig. 5*b*). With the two helices of FtsB in closer proximity, their conformation becomes even more similar to our previous model of an FtsB dimer (RMSD ~2 Å; Fig. S4*b*) (38).

A second important change that occurs in the TM region during the MD runs is a rearrangement and expansion of the hydrogen-bonding network. In the C-terminal section of FtsLB, there are 12 side chains in close proximity that are able to hydrogen-bond (three from each helix: Gln-16, Tyr-17, and Trp-20 in FtsB and three threonines, Thr-49, -52, and -56, in FtsL). With the exception of Trp-20, all of these side chains have both donor and acceptor groups. In addition, Gln-16 is also very flexible. Therefore, the network can rearrange in multiple configurations. Fig. 5*c* illustrates one of the configurations observed, which displays a total of seven interhelical hydrogen bonds. The configuration of the hydrogen-bonding network varies over the simulations, but some interactions are predominant during the runs (Table S2). The most persistent interaction is between Tyr-17 of FtsB subunit A and the side chain of Thr-52 of FtsL subunit C (Tyr-17 of subunit B prefers to interact with the backbone carbonyl of Leu-48). Gln-16 interacts primarily with the side chain hydroxyl groups of Thr-49 and Thr-52 from FtsL and with Gln-16 from the opposed FtsB helix. Trp-20 primarily donates to the side chain hydroxyl group of FtsL Thr-56, but it can also donate to the carbonyl group of Gln-16 side chain. This extended network of hydrogen bonds is likely to contribute significantly to the association of the TM region, which can form a stable oligomer in isolation *in vitro* (43).

As a control, we also performed a 160-ns simulation of a structural model that has comparably low energy but does not satisfy the evolutionary constraints in the TM region ("bad" model; Fig. S5*d*). The TM region rearranges away from the initial model relatively quickly, reaching an RMSD of >3 Å in the first 60 ns. Its average (2.8 Å) and maximum (3.5 Å) are higher than the RMSD of the TM region in the three replica runs of the "good" model (1.6, 1.9 and 2.3 Å, with maxima of 2.1, 2.4, and 2.7 Å, respectively).

A continuous FtsL helix and a dynamic coiled coil

Different sections of the coiled coil behave differently during the MD runs. These are notable in the helicity analysis presented in Fig. S6. The "extended coil" (the region that extends beyond the pattern of co-evolutionary contacts consistent with a coiled coil (Fig. 2)) unfolds partially as a bundle during the runs, although the region retains substantial helicity, and interactions still occur between pairs of FtsL and FtsB helices. The likely occurrence of a breakage of the helix between the "lower" and the "extended" coil regions was also hypothesized by a previous modeling analysis of the periplasmic region of the FtsLBQ complex (55). Interestingly, the location of the transition between these two regions roughly corresponds to the CCD.

The lower coil remains more stable during the run (final RMSD around 2.3, 3.4, and 2.9 Å). However, notable changes occur even in this region, providing further indication that the FtsLB complex may not be built to form a rigid, canonical, tetrameric coiled coil. Partial unfolding of the FtsL helix is observed in subunit C, and occasional unfolding is also notable in both FtsL subunits in the third replica run.

In the transition between the TM and coiled coil domains, the segment of 5–10 amino acids centered around the Gly-rich section of FtsB rapidly unfolds from the "unwound helix" conformation imposed by the modeling, unlinking the two domains and adopting a flexible and extended conformation (Fig. 5*a*). Conversely, the juxtamembrane region of FtsL remains stable as a continuous helix throughout the duration of all three replica runs. The unfolding of the Gly-rich linker of FtsB creates an opening that allows water to access the core of the four-helix bundle (Fig. 5*d*). Water molecules penetrate deeply up into the core of the coil, solvating the strongly polar side chains that would otherwise be buried in the structure (Arg-67 and Arg-74 from FtsL and Gln-39 and Asn-43 from FtsB, "polar core" in Fig. 5*d*). In this region near the membrane, the coil becomes essentially separated by the water into two two-helix bundles. Water is excluded from the above layer, where the four-helix bundle becomes compact again around a hydrophobic core consisting of Leu-46 from FtsB and Leu-77 and Trp-81 from FtsL ("hydrophobic core" in Fig. 5*d*).

With all caution in drawing conclusions from a theoretical model, it appears unlikely that a core so enriched in strongly polar amino acids would produce a very stable coiled coil. A possibility is that the stability of the coil is purposely "detuned" because the function of the FtsLB complex requires a weak coil, possibly to allow for a conformational change. A second hypothesis is that the region is actually designed to split into two separate two-helix coils. This split is most evident, as illustrated in the last frame of MD run number 3 (Fig. S5). A "split" coiled coil would be consistent with the observation that a solubilized version of the periplasmic region of FtsLB forced into a heterodimeric form binds to FtsQ with high affinity (49–51), suggesting that association with FtsQ may be mediated by two independent binding domains of FtsLB. Such an organization would designate the TM region as the major factor driving tetramerization.

Functional analysis: The effect of mutations in the TM region is consistent with the predicted interface

To investigate how the model's structural features support the function of FtsLB, a series of rationally designed variants of the complex were tested *in vivo* for their ability to support cell division. Because FtsL and FtsB are essential proteins, the mutant proteins were introduced into strains in which a chromosomal copy of the wildtype protein is under the control of a repressible promoter (45, 47). This allows for the depletion of the wildtype copy and the induction of the mutant version to reveal its phenotype. The expectation is that the most severe mutations will produce cells that elongate but are unable to divide, resulting in the formation of very long filaments, whereas less severe mutations will allow the cells to divide but will produce subpopulations of elongated cells. To assess each mutant, we measured the distri-

bution of cell lengths, as exemplified in Fig. 6*a* for the L15A mutant of FtsB. The data for each individual mutant are reported in Fig. S7.

Although none of the point mutations caused filamentous phenotypes, many produced elongated cells. To determine whether the difference between each mutant's and the wild-type's length distributions was significant, we used the Mann–Whitney *U* test (72). However, as a consequence of the very large sample size of each experiment (500 to >1,000 cells), minuscule differences can be statistically significant even if they are not biologically relevant. To overcome this issue, we adopted an operative classification based on the fraction of elongated cells observed for each variant. We defined as "elongated" those cells that are longer than the 95th percentile in the distribution of wildtype cell length (Fig. 6*a*). Based on this threshold, we defined phenotypes as "mild temperature–sensitive" (*Mild T.S.*) when >15% (*i.e.* >3-fold compared with the wildtype) of cells were elongated only at the less permissive temperature of 42 °C; as "mild" when >15% of cells were elongated at 37 °C; as "intermediate" when >25% of cells were elongated (>5-fold); as "severe" when over 50% of the cells were elongated (>10 fold); and, finally, as "filamentous" when all cells were filamentous. The example of Fig. 6*a*, which has 72% elongated cells at 37 °C, is therefore classified as "severe."

The fractions of elongated cells for each variant in the TM region of FtsL and FtsB are reported in Fig. 6*b*, with the relative classification reported at the *bottom*. The variants include a variety of drastic small-to-large amino acid changes (such as A10F in FtsB and L38W in FtsL), large-to-small changes (such as W14A and L8A in FtsB), and some conservative mutations (such as L19I in FtsB). We expected to observe division phenotypes when mutations affected the packing or hydrogen bonding at positions that mediate interaction between the helices. The results are in good agreement with this prediction. First, all positions that displayed impaired cell division phenotypes (Leu-8, Leu-12, Leu-15, Gln-16, and Trp-20 in FtsB; Leu-38 and Leu-42 in FtsL (Fig. 6*b*)) occur at the helix-helix interfaces, as illustrated schematically in Fig. 6*c*. In addition, all positions predicted to be away from the interface and exposed solely to lipids are classified as indistinguishable from wildtype (Leu-7, Ala-10, and Trp-14 in FtsB; Phe-43 and Ile-47 in FtsL). However, some of the TM region mutations that were predicted to be detrimental displayed little or no effect (*e.g.* Q16M, W20A, C45W, and T49W). This is particularly noticeable for the C-terminal side of the TM bundle, a section characterized by an extensive hydrogen bonding network (Fig. 5*c*). Mutations of Thr-49, Thr-52, and Thr-55 of FtsL and Tyr-17 of FtsB have no effect, and those of Gln-16 and Trp-20 of FtsB have little or no phenotype. Even a double mutation (Q16M/Y17F or Q16A/Y17F) that removes two hydrogen bonding groups is completely tolerated.

The finding is surprising because the C-terminal side of the TM bundle is the region with the highest number of co-evolutionary "connections," suggesting that these positions would be structurally or functionally important. Moreover, Gln-16 and Trp-20 of FtsB, are nearly absolutely conserved in proteobacteria (38). A potential explanation is that the hydrogen bonding network may be sufficiently robust, extensive, and plastic to accommodate changes. Because of the large network, the removal of some donors and acceptors may not be sufficiently detrimental to destabilize the complex. Conversely, the N-terminal region, which is mediated exclusively by packing of hydrophobic residues, could be more sensitive to disruption of the complementary side chain packing. It is also possible that thermodynamic stability of the TM region is not strictly required for function, at least in the conditions tested.

To investigate whether there is an overall correspondence between the observed biological phenotypes and predictions based on the structural model, we calculated mutational energies *in silico* for all TM mutants and compared them with the fraction of elongated cells observed for each variant (using the 42 °C data to maximize the dynamic range of the experimental observations). We calculated the energies using a rigid-body model without backbone movement as well as with FoldX, a method specifically calibrated to calculate the folding stability of protein mutants (73). The data are plotted in Fig. S8. The energies produced by FoldX statistically correlate with the severity of the phenotypes by rank order Spearman correlation coefficient analysis ($r = 0.4631$, $n = 29$, $p < 0.01$) (74). We conclude that perturbation of stability estimated on the basis of the structural model is a reasonably good predictor of the functional state of FtsLB.

The juxtamembrane and coiled coil of FtsB are tolerant to mutation

We applied a similar mutational approach to investigate the functional importance of the coiled coil and of the juxtamembrane region. The results are reported in Fig. 7 (and Fig. S7). We first tested whether the evolutionarily conserved Gly-rich juxtamembrane linker of FtsB (^{22}GKNG^{25}) is essential. A potential role for Gly is to provide structural flexibility, as suggested by our MD simulations. Alternatively, because of glycine's less restrictive Ramachandran distribution, this amino acid can also be required in a rigid structure to enable conformations of the backbone that are forbidden to all other amino acids.

We tested individual and double Gly-to-Ala mutations at positions 22 and 25. They presented either no defects (G22A and G22A/G25A) or a mild TS phenotype (G25A) (Fig. 7*a*). A possible explanation is that the structure of the linker retains sufficient flexibility even when Gly-22 and Gly-25 are substituted by Ala. To further test the flexibility of the linker, we inserted a series of Ala residues (up to three) between the TM domain and the coiled coil region (between positions Phe-21 and Gly-22), with the rationale that insertions should be better tolerated in a flexible region. The cells appear largely unaffected by the changes (only the two-Ala insertion mutation displays a mild TS phenotype; Fig. 7*b*). The outcome is therefore consistent with a flexible FtsB linker and confirms the presence of a helical break between the membrane and periplasmic domains of FtsB. These observations are not consistent with the alternative hypothesis that Gly is required to enable a rigid backbone conformation.

We also applied this Ala insertion strategy to test the coiled coil region of FtsB. A single additional Ala residue was inserted between the *b* and *c* positions (*i.e.* in a position that is solvent-

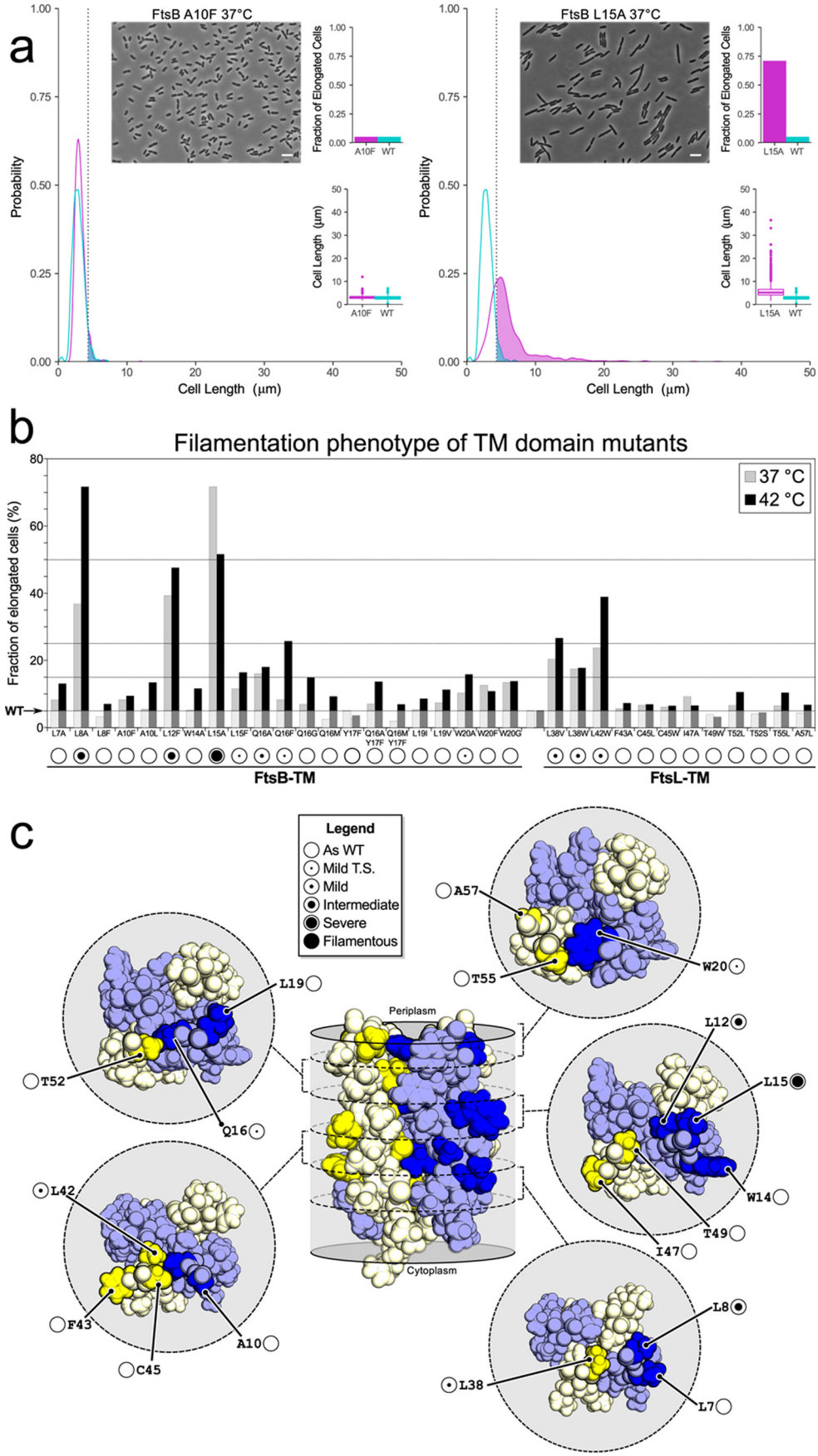

exposed) of each of the five heptad repeats. Most of these five insertion mutants did not display any impairment, with the exception of a mild TS phenotype for the second heptad insertion after position Ala-37 (Fig. 7*c*). Overall, the analysis suggests that the coiled coil of FtsB is likely to be quite plastic and able to tolerate insertion mutations all along its length.

Integrity of the juxtamembrane and coiled coil regions of FtsL is essential for function

Whereas the juxtamembrane and coiled coil domains of FtsB appeared tolerant to insertion, the opposite was observed for FtsL. We first introduced single, double, and triple Ala insertion mutations in the juxtamembrane region of FtsL (between positions Ala-57 and His-58). If the helix of FtsL is uninterrupted, the insertions should introduce strain into the structure because they would either produce a 100° rotation of the helix for each additional Ala or, more likely, introduce distortions into the helix. We observed that all insertion mutants, even the single Ala insertion, produced cells that were completely filamentous (Fig. 7, *b* and cell images in *c*). These are the most dramatic phenotypes observed in the whole study. The results are consistent with the hypothesis that FtsL forms an uninterrupted helix that runs through the membrane and periplasmic regions.

We also tested the juxtamembrane linker of FtsL with a series of point substitutions (H58A, H59A, and T60A; Fig. 7*a*). Interestingly, we observed some degree of functional disruption, particularly with the H59A mutation, which displays a 7-fold increase in the number of elongated cells compared with wildtype at 37 °C. In our model, His-59 is solvent-exposed and engaged only in minor interactions with the FtsB helix. It is possible that this position is important for interactions with other components of the divisome, possibly with the periplasmic domain of FtsQ, which was shown to cross-link with this region of FtsL (48).

Finally, we scanned the entire coiled coil region of FtsL by Ala insertion (Fig. 7*c*), as we did with FtsB. We observed a severe phenotype for the first heptad insertion, a mild phenotype for the second heptad insertion, and a wildtype phenotype for the third heptad insertion. A completely filamentous phenotype is then observed when Ala is inserted in the fourth heptad repeat (after position Arg-82). It is difficult to speculate what might cause such a dramatic defect, but we note that the mutation is in proximity to the CCD region of FtsL (residues 88–94, highlighted in *orange* in Fig. 7*e*). Insertion at position 89, which is within the CCD and which would correspond to the fifth heptad, if the coiled coil persisted in this region, produced a mild phenotype (~4-fold increase in elongated cells). Overall, the periplasmic coiled coil of FtsL is sensitive to mutation, whereas the same domain of FtsB is tolerant, as schematically illustrated in Fig. 7*e*. Interestingly, this outcome is the opposite of that observed for the mutagenesis of the TM region, where FtsB was the sensitive subunit, compared with the much milder phenotype displayed by FtsL (Fig. 6).

Conclusions

The topology of the FtsLB complex, a helical bundle spanning the membrane and periplasmic space, with terminal tails available for binding other components, is widely conserved evolutionarily (6, 50). The widespread occurrence of FtsLB across a broad variety of bacterial species with different cellular envelopes implies that this specific domain organization fulfills some important functional purpose, which is still unknown. To investigate this question, we have analyzed the structure-function relationship of the extended helical region of FtsLB, revealing a number of important features regarding the organization of the complex.

This study confirms that FtsLB is a higher-order oligomer and provides evidence that the complex consists of a heterotetramer. It identifies with a high degree of confidence the interface of the helical bundle region of the complex. It also produces a structural model of FtsLB validated experimentally through functional analysis. Further validation is also provided by a notable convergence of features in FtsB (the conformation of the TM helices and the presence of a flexible linker) that were also predicted in a prior model of FtsB based on a completely orthogonal set of experimental data (38).

The number of strongly polar, and even charged, amino acids that are predicted to be buried in the core of the coiled coil is a surprising and probably important finding, suggesting that the coil region may not be built for enhanced structural stability. A structural alternative to a monolithic four-helix coil could be the formation of two independent "dimeric" branches formed by one FtsL and one FtsB subunit. This possibility is consistent with previous observations that FtsLB fragments can bind to FtsQ with high affinity even when forced in a heterodimeric state (49–51).

We found that the integrity of the extended helix of FtsL is essential for the complex. A continuous helix is probably important for structural stability; given that the juxtamembrane linker of FtsB is disordered, a stable FtsL helix is probably necessary for nucleating the coiled coil. This hypothesis is in good agreement with the observation that amino acid insertions are most detrimental at the base of this domain. The helix of FtsL is also an interesting candidate for acting as a mechanical connection that could propagate a postulated allosteric conformational change (41, 42) across the periplasmic, TM, and cytoplasmic regions. For example, the cytoplasmic region of FtsL is important for the recruitment of FtsW (47); therefore, it is possible that FtsLB could control the activation of the

Figure 6. Mutations at the interface of the TM domain cause mild phenotypes *in vivo*. *a*, examples of *in vivo* analysis of point mutants with wildtype-like (A10F) and defective (L15A) phenotypes. The distribution of cells lengths is compared between the wildtype (*aqua*) and the mutant (*magenta*). L15A displays 72% of cells that are longer than the 95th percentile in the wildtype distribution (*colored areas*, *past* the *dotted line*). As such, it is classified as a "severe" mutation. Graphs for each individual mutant are provided and explained in detail in Fig. S7. *Scale bar*, 5 μm. *b*, phenotypes of TM domain mutants at 37 and 42 °C growth conditions. Classification is indicated using *filled circles below*. *Filamentous*, all cells are elongated at 37 °C; *Severe*, >50% of the cells are elongated; *Intermediate*, >25% of cells are elongated at 42 °C; *Mild*, >15% of cells are elongated at 42 °C; mild temperature-sensitive (*Mild T.-S.*), >15% of cells are elongated at 42 °C. *c*, location of the mutations within the structure of the TM domain. All mutations that display a cell division phenotype map within the interface of the helical bundle. All mutations on the outer surface of the bundle display *As WT* phenotypes.

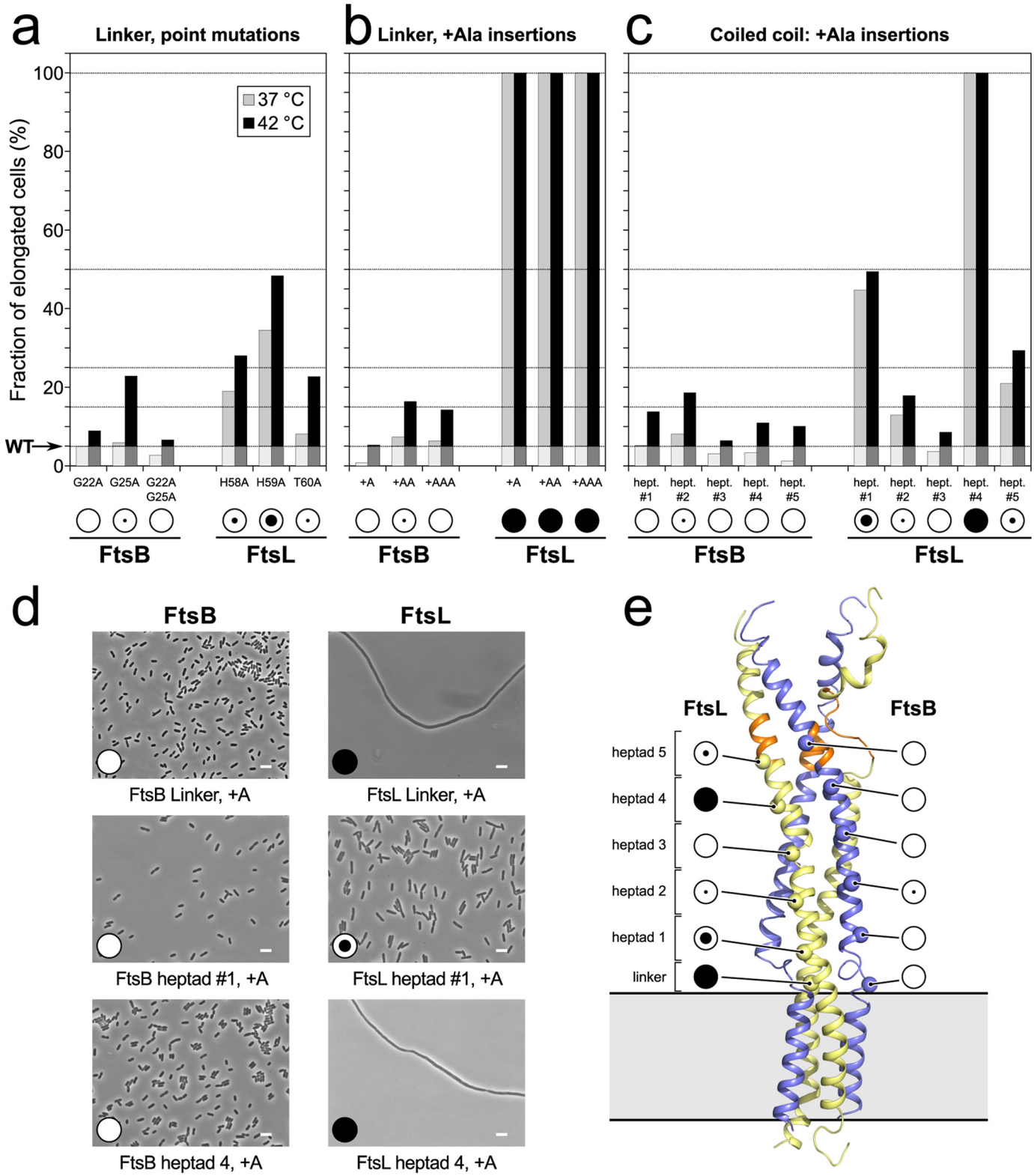

Figure 7. The juxtamembrane and coiled coil regions of FtsL are sensitive to mutation. *a*, phenotypic analysis of juxtamembrane ("linker" region) point mutations of FtsL and FtsB, classified as detailed in the legend to Fig. 6. Graphs for each individual mutant are provided in Fig. S7. *b*, alanine insertion mutation (1–3 extra residues) in the same region. *c*, Ala insertion mutations in the coiled coil region (operated between positions *b* and *c* in the heptad repeats). *d*, representative images of Ala insertion mutants in the linker and periplasmic coiled coil of FtsB and FtsL. Images for all mutants are provided in Fig. S7. *e*, observed phenotype of the mutants mapped onto the molecular model. Constriction control domain is displayed in *orange*. The evidence is consistent with a flexible linker in FtsB, with the presence of a helical break, and with an uninterrupted helix that runs through the membrane and periplasmic regions for FtsL.

FtsWI peptidoglycan synthase complex through direct interaction by coordinating a signal from the periplasm (*i.e.* interaction with FtsN). This study provides the structural groundwork necessary for investigating this and other hypotheses with coordinated biophysical and functional studies, which are necessary to finally clarify the precise role and the molecular mechanisms of the FtsLB complex in bacterial cell division.

Experimental procedures

Co-evolutionary analysis

Sequences of FtsL and FtsB homologues were collected using the DELTA-BLAST algorithm on the RefSeq database (75). These sequences were filtered to include only proteobacterial species and then concatenated by matching the organism name in each record. The paired sequences were then aligned using the ClustalW algorithm with five guide tree and five hidden Markov model iterations (76). Columns in the alignment with a gap fraction higher than 0.3 were masked. This paired multisequence alignment was analyzed with the EV-Couplings algorithm (56) using default parameters and ignoring membrane topology, which would otherwise assume that sequential TM domains are anti-parallel. The top 95 (the number of unmasked columns in the multisequence alignment divided by 2) evolutionary constraints (*i.e.* the co-varying residues) predicted by EV-Fold between FtsL and FtsB were used for analysis and molecular modeling. The paired alignment is provided as a supplementary FASTA file. A total of 1291 sequences were used in the alignment. The number of effective sequences after reweighting for similarity is 883.1, corresponding ~4.6 sequences/residue. From this, ~40% of the top 95 contacts are estimated to be false positive pairs in the co-evolutionary analysis (77).

Modeling the TM region of FtsLB

All modeling was performed using programs written in the Molecular Software Library (MSL) (78). For the TM domain, ideal helices corresponding to residues 1–21 of FtsB and residues 35–58 of FtsL were generated. C_2 rotational symmetry (or C_3, in the case of the hexamer) was preserved around the z axis for FtsB helices and FtsL helices. The geometry of the FtsL and FtsB bundles was defined by the following parameters: interhelical distance (d); rotation around the helical axis (ω); crossing angle (θ), and position of the crossing point (s). Additionally, the orientation of the FtsL and FtsB bundles were changed by operating a rotation (Ω) and a translation (S) of each helix bundle about the z axis.

Starting from an initial random assignment of the parameters, the FtsLB TM helix complex was optimized using a Monte Carlo procedure that altered the interhelical geometry. The conformation of the side chains was periodically optimized with a 5% probability after each move. Side chain optimization was performed with a greedy trials algorithm using the backbone-dependent Energy-Based Conformer Library (bEBL) applied at the SL80 level (79, 80). Energies were calculated using the CHARMM 22 van der Waals function (81) and the hydrogen-bonding function of SCWRL 4 (82) as implemented in MSL. Additionally, sigmoidal distance restraints were placed between the Cα atoms of each pair of top co-evolving positions (83), using the following form,

$$E_{\text{sigmoid}} = \frac{w}{1 + e^{-a(r - r_0)}} + C \qquad \text{(Eq. 1)}$$

where $E_{\text{sigmoidal}}$ is the additional energy term, w is the weight, a is the slope, C is the intercept, r is the distance between the atoms, and r_0 is the distance cutoff. For these experiments, w was set to 10 kcal/mol, a was set to 0.5 Å^{-1}, C was set to −2.5 kcal/mol, and r_0 was set to 10 Å.

For each pair of co-evolving residues, there are multiple pairs in the complex corresponding to the same residues on different chains. Only the restraints with the lowest energies for each pair were added to the energy score, whereas the remaining ones were masked. The evolutionary constraints are listed in Table S1. Models were sorted by energy and clustered using a greedy algorithm and a Cα RMSD threshold of 2.5.

As a negative control for the molecular dynamics simulations, a second model of the TM domain was produced by identifying a conformation with comparable energy of the initial model but with poor agreement with the co-evolutionary data (bad model). In this model, only one pair of co-evolving positions had a minimum heavy atom distance below 5 Å, and only two pairs had Cα distances below 10 Å, whereas all pairs satisfy these conditions in the good model.

In silico mutational energies for the mutants in the transmembrane region were calculated in two ways. Rigid-backbone repacking was performed using MSL. Point mutations of interest were generated, and neighboring side chains were repacked using 100 rounds of a greedy trials algorithm. Mutated residues were repacked at the SL99 conformer level of the bEBL library; residues within 8, 16, and 20 Å were repacked at the SL95, SL90, and SL80 levels, respectively. van der Waals radii were scaled by 0.8. Energies of the mutants were subtracted from that of the wildtype to calculate their $\Delta\Delta E$. Mutations were also analyzed using the FoldX Suite (73). The models were first energy-minimized using the *RepairPDB* command with the membrane parameter set to true. Mutant $\Delta\Delta G$ calculations were performed using the *buildModel* command with the membrane parameter set to true.

Modeling the coiled coil domains of FtsL and FtsB

Supercoiled helices corresponding to residues 52–94 of FtsL and 21–63 of FtsB were generated by using a coiled coil generator based on a coiled coil parameterization described previously (84). The superhelical radius (r_1), superhelical pitch (P), helical rotation (Φ_1), and z-shift (s) of both FtsL and FtsB were freely altered, whereas the rise per residue (h) and helical radius (r_0) were kept constant. Additionally, the orientation of the FtsL and FtsB bundles were changed by operating a rotation (Ω) and a translation (S) of each helix bundle about the z axis. C_2 symmetry (C_3 for the hexamer) was preserved within the FtsL backbones and the FtsB backbones.

The coiled coils were optimized using a Monte Carlo procedure, changing their superhelical parameters starting from an initial assignment of random parameters. Side-chain conformational sampling was performed with a variable number of

conformers with the positions that participate at a canonical coiled coil interface receiving higher sampling; the *a* and *d* positions were sampled at the SL80 conformer level of the bEBL library, *e* and *g* positions at the SL75 level, *b* and *c* at the SL70 level, and *f* at the SL60 level. Energies were calculated based on CHARMM 22 van der Waals and CHARMM 22 electrostatic terms. Additionally, sigmoidal restraints for each co-evolving pair in the coiled coil region were added, as described above.

Modeling the juxtamembrane regions of FtsL and FtsB

Top models of the TM and coiled coil domains were connected by aligning the helical residues 52–58 of FtsL, which were present in the models of both regions. The RMSD between the Cα atoms of these residues was minimized while keeping the main axis of both domains parallel to and centered on the *z* axis. The juxtamembrane regions of FtsL and FtsB were then replaced with loops corresponding to fragments from the PDB, as described previously (38). For FtsB, six-residue loops, corresponding to positions 21–26, with four flanking helical residues on each side, were used, with an additional sequence requirement that the fragment contain at least one glycine. For FtsL, 15-residue fragments with four flanking helical residues on each side were used with the requirement that the loop have helical secondary structure. Long helix fragments were used to better distribute minor deviation in alignment between the transmembrane and coiled coil helices. The connecting regions were optimized based on a greedy trials algorithm to minimize steric clashing, and the final model was minimized using BFGS constrained optimization using CHARMM (85). Structural voids were analyzed using BetaCavityWeb (86). For the creation of the bad model, the TM model that did not satisfy the co-evolutionary constraints was aligned and connected to the same model of the coiled coil domain using an identical procedure.

All-atom molecular dynamic simulations

For the molecular dynamics simulations, the model's coiled coil region was extended, to avoid edge effects, to residues 110 (FtsL) and 79 (FtsB). The cytoplasmic side of FtsL was also extended to include residues 30–34, modeled in ideal α-helix. Four all-atom MD simulations (a 260-ns run, two 200-ns replica runs, and a 160-ns control run on the control bad model) were performed using the CHARMM 36 force field and NAMD version 2.10 software (87, 88). CHARMM-GUI membrane builder (89) was used to prepare systems composed of a POPE bilayer consisting of 301 lipids, the FtsLB tetramer, an ionic concentration of 0.150 M NaCl, and 59,034 TIP3P water molecules for hydration. The sizes of the boxes at the beginning of the simulation were $\sim 97 \times 97 \times 242$ Å^3 for runs 1, 2, and 3 and $97 \times 97 \times 245$ Å^3 for the control run. The simulations were initially minimized and equilibrated for 75 ps at an integration time of 1 fs/step and for 600 ps at an integration time of 2 fs/step. The integration time step for the production runs of each of the systems was 2.0 fs/step. The simulations were carried out in the NPT ensemble at a pressure of 1 atmosphere and a temperature of 310.15 K, using the Nose–Hoover Langevin piston and Langevin dynamics method. Particle mesh Ewald was used for electrostatic interactions, and a 12-Å cutoff was applied to Lennard–Jones interactions with a switching function from 10 to 12 Å. The RMSD analysis was performed using the RMSD trajectory tool in VMD (90). Hydrogen-bonding analysis was performed with an in-house script.

Helicity analysis was performed by measuring the backbone dihedrals and the distance between O_i and N_{i+4} for each residue in each selected frame of the simulation. If the O_i–N_{i+4} distance was between 2.0 and 4.2 Å and the backbone dihedral angles were within the favored α-helical region as defined in PROCHECK (91), the residue was classified as helical. If the O_i–N_{i+4} distance was within 5 Å and the backbone dihedral angles were within either the favored or allowed α-helical region, the residue was classified as near-helical. Otherwise, the residue was classified as non-helical.

Cloning, expression, purification, and labeling of FtsLB constructs for FRET measurements

The His-tagged FtsB and Strep-tagged Cys-less (C41A and C45A) FtsL(35–121) (Table S3) were introduced into a modified pETDuet-1 vector at restriction sites NcoI/HindIII and NdeI/XhoI, respectively. For fluorophore labeling, cysteine mutations were introduced either to FtsB (S97C) or to Cys-less FtsL (I100C) via QuikChange mutagenesis (Novagene). All constructs were confirmed by DNA sequencing (Quintarabio).

The plasmids were transformed into BL21 (DE3) cells. Individual colonies were picked and grown overnight in 3 ml of LB broth containing 100 μg/ml of ampicillin before being diluted 1:500 in 1 liter of ZYP-5052 autoinduction medium as described (92), and grown at 37 °C until reaching an A_{600} of 0.8, after which it was incubated for an additional 20 h at 25 °C. The cells were then lysed by sonication in 10 ml/g lysis buffer (50 mM NaCl, 50 mM HEPES, 10 mM TCEP, brought to pH 7.0 with NaOH) supplemented with 0.25 mg/ml lysozyme, 5 mM β-mercaptoethanol, and 1 mM phenylmethylsulfonyl fluoride. The inclusion body fraction was separated by centrifugation at 10,000 $\times$ *g* for 20 min, followed by ultracentrifugation of the supernatant at 130,000 $\times$ *g* for 30 min to isolate the cell membranes. The FtsLB complex was then extracted from the membrane fraction with lysis buffer supplemented with 18 mM *n*-decyl-β-D-maltopyranoside (DM; Anatrace) and 10 mM TCEP, rocking at 4 °C overnight. Solubilized protein was added to 3 ml of Ni-NTA-agarose resin (Qiagen) and rocked for 2 h at 4 °C before the resin was washed and the complex was labeled on-column with either Cy3 or Cy5 maleimide (Lumiprobe) for FtsB or FtsL. On-column fluorophore labeling was performed by running 3 column volumes of Ni wash buffer (300 mM NaCl, 25 mM HEPES, pH 8.0, 50 mM imidazole, 10 mM TCEP, brought to pH 7.0 with NaOH) supplemented with 5.4 mM DM, 3 column volumes Cy3 or Cy5 labeling buffer (100 μM Cy3 or Cy5 maleimide, 5.4 mM DM, 50 mM NaCl, 50 mM HEPES, pH 8.0, brought to pH 7.0 with NaOH), 6 column volumes of Ni wash buffer supplemented with 450 μM *n*-dodecyl-β-D-maltoside (DDM; Avanti Polar Lipids), and 2 column volumes of elution buffer (300 mM NaCl, 25 mM HEPES, pH 8.0, 450 μM DDM, 300 mM imidazole, brought to pH 7.0 with NaOH). For quantification, the elution fractions were dialyzed overnight at 4 °C against FRET buffer (300 mM NaCl, 25 mM HEPES pH 8.0, 450 μM DDM, brought to pH 7.0 with NaOH).

Labeling efficiency of each fraction was quantified by UV-visible spectroscopy, using absorbance at 280 nm (protein), 550 nm (Cy3), and 650 nm (Cy5). First, the concentration of the protein was calculated, taking into account the absorbance of the fluorophore,

$$[\text{Protein}] = \frac{A_{280} - (A_{Cy} \times CF_{Cy})}{\epsilon_{280}} \quad \text{(Eq. 2)}$$

where A_{280} is the absorbance at 280 nm, A_{Cy} is the absorbance at 550 nm (Cy3-labeled samples) or 650 nm (Cy5-labeled samples), ϵ_{280} is the molar extinction coefficient of FtsLB at 280 nm (32,430 M^{-1} cm^{-1}), and CF_{Cy} is the appropriate correction factor (CF_{Cy3} = 0.11 and CF_{Cy5} = 0.05) to subtract the contribution of the fluorophore to absorbance at 280 nm. Then the labeling efficiency P_{Cy} was calculated according to the following,

$$P_{Cy} = \frac{A_{Cy}}{[\text{Protein}] \times \epsilon_{Cy}} \quad \text{(Eq. 3)}$$

where ϵ_{Cy} is the molar extinction coefficient of the fluorophore (ϵ_{Cy3} = 150,000 M^{-1} cm^{-1} at 550 nm, ϵ_{Cy5} = 250,000 M^{-1} cm^{-1} at 650 nm). Cysteine-less versions of the FtsL and FtsB constructs were also purified and labeled three times with the same protocol to determine background labeling, which was negligible.

A second round of purification could be performed by loading the Ni-NTA–purified FtsLB complex over a streptavidin column. The most concentrated Ni-NTA elution fractions were added to 3 ml of streptavidin resin and rocked for 2 h at 4 °C before being washed with 3 column volumes of streptavidin buffer (20 mM Tris, 300 mM NaCl, 0.1 mM EDTA, 0.5 mM TCEP, brought to pH 8.0 with NaOH) with 450 μM DDM, followed by elution with 3 column volumes of streptavidin buffer plus 2.5 mM desthiobiotin (initially dissolved in 1 ml of DMSO) and 450 μM DDM. Samples from each fraction of the nickel and streptavidin column were boiled in 4× SDS-PAGE loading buffer before being run on NuPage 4–12% BisTris protein gels at 150 V for 1 h (Thermo Fisher Scientific). Because the FtsLB complex obtained after Ni-NTA had sufficient purity for FRET studies, this second chromatography was not routinely performed, but it was used initially to confirm the stability of the FtsLB complex.

FRET measurements

In all experiments, the FtsLB complex was diluted to 1.35 μM in FRET buffer, which contains 450 μM DDM, for a final protein/detergent molar ratio of 1:333. Experiments were performed by labeling either the FtsL moiety (FtsL-C41A/C45A/I100C + FtsB) or the FtsB moiety (FtsL-C41A/C45A + FtsB-S97C) in the protein complex. All FRET analysis was performed on an M1000 Tecan plate reader, with excitation set at 550 nm and emission recorded from 560 to 800 nm in 1-nm increments.

The formation of FtsL-FtsB oligomers *in vitro* was assessed by measuring FRET on a 50:50 mix of $FtsL_{Cy3}$-$FtsB_{unlabeled}$ and $FtsL_{unlabeled}$-$FtsB_{Cy5}$ complexes, which were compared with a 50:50 mix of $FtsL_{Cy3}$-$FtsB_{unlabeled}$ and $FtsL_{unlabeled}$-$FtsB_{unlabeled}$ (donor-only sample) complexes and a 50:50 mix of $FtsL_{unlabeled}$-$FtsB_{Cy5}$ and $FtsL_{unlabeled}$-$FtsB_{unlabeled}$ (acceptor-only sample) complexes.

The stoichiometric analysis of FtsL was performed by mixing $FtsL_{Cy3}$-$FtsB_{unlabeled}$ (donor) and $FtsL_{Cy5}$-$FtsB_{unlabeled}$ (acceptor) samples in different ratios, from 20:80 donor/acceptor up to 90:10, in 10% increments. To determine donor fluorescence in the absence of the acceptor, equivalent samples were produced by mixing $FtsL_{Cy3}$-$FtsB_{unlabeled}$ (donor) and $FtsL_{unlabeled}$-$FtsB_{unlabeled}$ (unlabeled) in the same molar ratios. The stoichiometric analysis of FtsB was performed similarly. Donor (Cy3) fluorescence was recorded using its peak emission at 570 nm. Quenching (Q) of the donor fluorophore was calculated, as explained below, according to Equation 6, from donor/acceptor-labeled protein sample mixes (F) and donor/unlabeled protein sample mixes (F_0). Each experiment was independently replicated at least five times.

Fitting of experimental FRET data to obtain the number of subunits

Fitting for different oligomeric states was performed as described by Adair and Engelman (68),

$$Q = \left(1 - \frac{f_Q}{f_D}\right)(1 - P_D^{n-1}) \quad \text{(Eq. 4)}$$

where Q is related to the molar fluorescence of the quenched donor (f_Q) in the presence of the acceptor, the molar fluorescence of the donor f_D in the absence of acceptor, the number of subunits in the oligomer n, and the molar fraction of donor-labeled protein P_D.

P_D was calculated as follows,

$$P_D = \frac{[\text{D}]}{[\text{D}] + [\text{A}]} \quad \text{(Eq. 5)}$$

where [D] is the molar concentration of donor-labeled protein and [A] is the molar concentration of acceptor-labeled protein.

Relative quenching was calculated as follows,

$$Q = 1 - \frac{F}{F_0} \quad \text{(Eq. 6)}$$

where F is the experimentally measured quenched fluorescence for a certain donor/acceptor molar fraction and F_0 is the experimentally measured unquenched fluorescence of the same amount of donor, obtained in the absence of acceptor and in the presence of an equivalent amount of unlabeled protein. In Equation 4, the quantity related to the molar fluorescence can be treated as an overall unknown constant k.

$$\left(1 - \frac{f_Q}{f_D}\right) = k \quad \text{(Eq. 7)}$$

The parameter k was thus fit using a least square procedure to the experimental data Q as a function of donor fraction P_D according to Equation 8 for the different oligomeric states n.

$$Q(P_D) = k(1 - P_D^{n-1}) \quad \text{(Eq. 8)}$$

The relative quality of the fits to different oligomeric states was assessed by comparing the sum of the squared residuals between the experimental data and the models.

Bacterial strains, plasmids, and media for in vivo experiments

The phenotypic analysis was performed using depletion strain NB946 for FtsB (7) and MDG277 for FtsL (45). For all experiments described, bacterial cells were grown in LB medium supplemented with 100 μg/ml spectinomycin (Dot Scientific) and the appropriate carbon source. Medium was supplemented with 0.2% (w/v) L-arabinose (Sigma) or 0.2% (w/v) D-glucose (Sigma) to induce or repress, respectively, the expression of chromosomal copies of the wildtype genes regulated by the PBAD promoter. 20 μM isopropyl-β-D-1-thiogalactoside was added to the media to induce the expression of mutant genes regulated by the pTrc promoter in the plasmid. Point mutants and insertion mutants of FtsL and FtsB were constructed in plasmid pNG162 (45) using either standard QuikChange mutagenesis or inverse PCR mutagenesis.

Depletion strain experiments

The protocol for the depletion strain experiment was adapted from Gonzalez and Beckwith (45). In short, a mutated copy of FtsB or FtsL was transformed into its respective depletion strain. Strains were grown overnight at 37 °C on an LB plate supplemented with arabinose and spectinomycin. A single colony from the plate was grown overnight at 37 °C in 3 ml of LB medium supplemented with arabinose and spectinomycin. The overnight culture was then diluted 1:100 into fresh LB medium containing the same supplement and grown to an A_{600} of ~0.3. An aliquot of 1 ml of culture was washed twice with LB medium lacking any sugar and then diluted 1:100 into 3 ml of fresh LB medium supplemented with glucose and isopropyl-β-D-1-thiogalactoside to induce the expression of the mutated gene and the repression of the wildtype gene. The cells were then grown at 37 or 42 °C for 3.5 h before microscopy, the approximate time necessary to deplete the cells of the wildtype chromosomal copy (45). Depletion strains provided with their respective wildtype copy of the protein in the plasmid were tested as positive controls, and, similarly, depletion strains with no protein in the plasmid (empty vector) were tested as negative controls.

Microscopy and cell length measurement

10 μl of cell samples were mounted on a number 1.5, 24 × 50-mm (0.16–0.19-mm thickness) coverglass slide (Fisher). Cells were cushioned with a 3% (w/v) agarose gel pad to restrict the movement of the live cells. Cells were optically imaged using a Nikon Eclipse Ti inverted microscope equipped with crossed polarizers and a Photometrics CoolSNAP HQ2 CCD camera using a Nikon ×100 oil objective lens. Phase-contrast images of bacterial cells were recorded with a 70-ms exposure time using Nikon NIS Elements software. Multiple snapshots were collected for each experiment. All images were analyzed to measure the cell length in Oufti (93) using one single optimized parameter set.

Whole-cell lysate preparation and Western blotting

Expression level across all variants was assessed by Western blot analysis (Fig. S9). 3.0 ml of cells were pelleted and resuspended in 500 μl of sonication buffer (25 mM Tris-HCl, 2 mM EDTA, pH 8.0). The cells were sonicated and centrifuged at 16,000 × *g* for 5 min before collecting the supernatant. Total protein concentration was determined by BCA assay (Pierce). 150 μl of lysates were mixed with 50 μl of 4× LDS sample buffer (Novex, Life Technologies) and boiled at 95 °C for 5 min. For each sample, the equivalent of 10 μg of total protein was separated by SDS-PAGE (Invitrogen) and transferred to polyvinylidene difluoride membrane (VWR). Horseradish peroxidase-tagged anti-FLAG (M2) antibodies (Sigma; 1:1,000) were used for immunoblotting analysis.

Author contributions—S. G. C., D. -A. M., C. R. A., G. D. -V., and A. S. conceptualization; S. G. C., D. -A. M., and A. S. data curation; S. G. C. and A. S. software; S. G. C., D. -A. M., C. R. A., G. D. -V., and A. S. formal analysis; S. G. C., D. -A. M., C. R. A., G. D. -V., S. J. C., and A. S. investigation; S. G. C., D. -A. M., C. R. A., L. M. L., A. S. K., R. C., J. A. C., N. R., D. B. W., A. A. H., J. L. R., Q. C., and A. S. methodology; S. G. C., D. -A. M., C. R. A., G. D. -V., and A. S. writing-original draft; S. G. C., D. -A. M., C. R. A., G. D. -V., S. J. C., and A. S. writing-review and editing; C. R. A. validation; D. B. W., A. A. H., J. L. R., Q. C., and A. S. supervision; A. S. funding acquisition; A. S. project administration.

Acknowledgments—We thank Drs. Jon Beckwith and Mark Gonzalez for kindly providing plasmids and strains for the in vivo analysis and for guidance in performing the experiments. Computational resources from the Extreme Science and Engineering Discovery Environment (XSEDE), supported by National Science Foundation Grant OCI-1053575, are greatly appreciated. We thank Dr. Kai Cai for assistance during the biophysical studies and Dr. Elizabeth Caselle for critical reading of the manuscript.

References

1. Wang, L., Khattar, M. K., Donachie, W. D., and Lutkenhaus, J. (1998) FtsI and FtsW are localized to the septum in *Escherichia coli*. *J. Bacteriol.* **180,** 2810–2816 Medline
2. Hale, C. A., and de Boer, P. A. J. (2002) ZipA is required for recruitment of FtsK, FtsQ, FtsL, and FtsN to the septal ring in *Escherichia coli*. *J. Bacteriol.* **184,** 2552–2556 CrossRef Medline
3. Hale, C. A., and de Boer, P. A. (1999) Recruitment of ZipA to the septal ring of *Escherichia coli* is dependent on FtsZ and independent of FtsA. *J. Bacteriol.* **181,** 167–176 Medline
4. Liu, Z., Mukherjee, A., and Lutkenhaus, J. (1999) Recruitment of ZipA to the division site by interaction with FtsZ. *Mol. Microbiol.* **31,** 1853–1861 CrossRef Medline
5. Chen, J. C., and Beckwith, J. (2001) FtsQ, FtsL and FtsI require FtsK, but not FtsN, for co-localization with FtsZ during *Escherichia coli* cell division. *Mol. Microbiol.* **42,** 395–413 CrossRef Medline
6. Buddelmeijer, N., and Beckwith, J. (2004) A complex of the *Escherichia coli* cell division proteins FtsL, FtsB and FtsQ forms independently of its localization to the septal region. *Mol. Microbiol.* **52,** 1315–1327 CrossRef Medline
7. Buddelmeijer, N., Judson, N., Boyd, D., Mekalanos, J. J., and Beckwith, J. (2002) YgbQ, a cell division protein in *Escherichia coli* and *Vibrio cholerae*, localizes in codependent fashion with FtsL to the division site. *Proc. Natl. Acad. Sci. U.S.A.* **99,** 6316–6321 CrossRef Medline
8. Mercer, K. L. N., and Weiss, D. S. (2002) The *Escherichia coli* cell division protein FtsW is required to recruit its cognate transpeptidase, FtsI (PBP3), to the division site. *J. Bacteriol.* **184,** 904–912 CrossRef Medline
9. Schmidt, K. L., Peterson, N. D., Kustusch, R. J., Wissel, M. C., Graham, B., Phillips, G. J., and Weiss, D. S. (2004) A predicted ABC transporter, FtsEX,

is needed for cell division in *Escherichia coli*. *J. Bacteriol.* **186,** 785–793 CrossRef Medline
10. Goehring, N. W., Gueiros-Filho, F., and Beckwith, J. (2005) Premature targeting of a cell division protein to midcell allows dissection of divisome assembly in *Escherichia coli*. *Genes Dev.* **19,** 127–137 CrossRef Medline
11. Goehring, N. W., Gonzalez, M. D., and Beckwith, J. (2006) Premature targeting of cell division proteins to midcell reveals hierarchies of protein interactions involved in divisome assembly. *Mol. Microbiol.* **61,** 33–45 CrossRef Medline
12. Ghigo, J. M., Weiss, D. S., Chen, J. C., Yarrow, J. C., and Beckwith, J. (1999) Localization of FtsL to the *Escherichia coli* septal ring. *Mol. Microbiol.* **31,** 725–737 CrossRef Medline
13. Lutkenhaus, J., Pichoff, S., and Du, S. (2012) Bacterial cytokinesis: From Z ring to divisome. *Cytoskeleton* **69,** 778–790 CrossRef Medline
14. de Boer, P. A. J. (2010) Advances in understanding E. coli cell fission. *Curr. Opin. Microbiol.* **13,** 730–737 CrossRef Medline
15. Erickson, H. P., Anderson, D. E., and Osawa, M. (2010) FtsZ in bacterial cytokinesis: cytoskeleton and force generator all in one. *Microbiol. Mol. Biol. Rev.* **74,** 504–528 CrossRef Medline
16. Bisson-Filho, A. W., Hsu, Y.-P., Squyres, G. R., Kuru, E., Wu, F., Jukes, C., Sun, Y., Dekker, C., Holden, S., VanNieuwenhze, M. S., Brun, Y. V., and Garner, E. C. (2017) Treadmilling by FtsZ filaments drives peptidoglycan synthesis and bacterial cell division. *Science* **355,** 739–743 CrossRef Medline
17. Yang, X., Lyu, Z., Miguel, A., McQuillen, R., Huang, K. C., and Xiao, J. (2017) GTPase activity-coupled treadmilling of the bacterial tubulin FtsZ organizes septal cell wall synthesis. *Science* **355,** 744–747 CrossRef Medline
18. Ortiz, C., Natale, P., Cueto, L., and Vicente, M. (2016) The keepers of the ring: regulators of FtsZ assembly. *FEMS Microbiol. Rev.* **40,** 57–67 CrossRef Medline
19. Haney, S. A., Glasfeld, E., Hale, C., Keeney, D., He, Z., and de Boer, P. (2001) Genetic analysis of the *Escherichia coli* FtsZ. ZipA interaction in the yeast two-hybrid system: characterization of FtsZ residues essential for the interactions with ZipA and with FtsA. *J. Biol. Chem.* **276,** 11980–11987 CrossRef Medline
20. Szwedziak, P., Wang, Q., Freund, S. M., and Löwe, J. (2012) FtsA forms actin-like protofilaments. *EMBO J.* **31,** 2249–2260 CrossRef Medline
21. Du, S., Pichoff, S., and Lutkenhaus, J. (2016) FtsEX acts on FtsA to regulate divisome assembly and activity. *Proc. Natl. Acad. Sci. U.S.A.* **113,** E5052–E5061 CrossRef Medline
22. Yang, D. C., Peters, N. T., Parzych, K. R., Uehara, T., Markovski, M., and Bernhardt, T. G. (2011) An ATP-binding cassette transporter-like complex governs cell-wall hydrolysis at the bacterial cytokinetic ring. *Proc. Natl. Acad. Sci. U.S.A.* **108,** E1052–E1060 CrossRef Medline
23. Männik, J., Bailey, M. W., O'Neill, J. C., and Männik, J. (2017) Kinetics of large-scale chromosomal movement during asymmetric cell division in *Escherichia coli*. *PLoS Genet.* **13,** e1006638 CrossRef Medline
24. Aarsman, M. E. G., Piette, A., Fraipont, C., Vinkenvleugel, T. M. F., Nguyen-Distèche, M., and den Blaauwen, T. (2005) Maturation of the *Escherichia coli* divisome occurs in two steps. *Mol. Microbiol.* **55,** 1631–1645 CrossRef Medline
25. Vollmer, W., and Bertsche, U. (2008) Murein (peptidoglycan) structure, architecture and biosynthesis in *Escherichia coli*. *Biochim. Biophys. Acta* **1778,** 1714–1734 CrossRef Medline
26. Cho, H., Wivagg, C. N., Kapoor, M., Barry, Z., Rohs, P. D. A., Suh, H., Marto, J. A., Garner, E. C., and Bernhardt, T. G. (2016) Bacterial cell wall biogenesis is mediated by SEDS and PBP polymerase families functioning semi-autonomously. *Nat. Microbiol.* **1,** 16172 CrossRef Medline
27. Meeske, A. J., Riley, E. P., Robins, W. P., Uehara, T., Mekalanos, J. J., Kahne, D., Walker, S., Kruse, A. C., Bernhardt, T. G., and Rudner, D. Z. (2016) SEDS proteins are a widespread family of bacterial cell wall polymerases. *Nature* **537,** 634–638 CrossRef Medline
28. Emami, K., Guyet, A., Kawai, Y., Devi, J., Wu, L. J., Allenby, N., Daniel, R. A., and Errington, J. (2017) RodA as the missing glycosyltransferase in *Bacillus subtilis* and antibiotic discovery for the peptidoglycan polymerase pathway. *Nat. Microbiol.* **2,** 16253 CrossRef Medline
29. Mohammadi, T., Sijbrandi, R., Lutters, M., Verheul, J., Martin, N. I., den Blaauwen, T., de Kruijff, B., and Breukink, E. (2014) Specificity of the transport of lipid II by FtsW in *Escherichia coli*. *J. Biol. Chem.* **289,** 14707–14718 CrossRef Medline
30. Mohammadi, T., van Dam, V., Sijbrandi, R., Vernet, T., Zapun, A., Bouhss, A., Diepeveen-de Bruin, M., Nguyen-Distèche, M., de Kruijff, B., and Breukink, E. (2011) Identification of FtsW as a transporter of lipid-linked cell wall precursors across the membrane. *EMBO J.* **30,** 1425–1432 CrossRef Medline
31. Yang, J.-C., Van Den Ent, F., Neuhaus, D., Brevier, J., and Löwe, J. (2004) Solution structure and domain architecture of the divisome protein FtsN. *Mol. Microbiol.* **52,** 651–660 CrossRef Medline
32. Di Lallo, G., Fagioli, M., Barionovi, D., Ghelardini, P., and Paolozzi, L. (2003) Use of a two-hybrid assay to study the assembly of a complex multicomponent protein machinery: bacterial septosome differentiation. *Microbiology* **149,** 3353–3359 CrossRef Medline
33. Karimova, G., Dautin, N., and Ladant, D. (2005) Interaction network among *Escherichia coli* membrane proteins involved in cell division as revealed by bacterial two-hybrid analysis. *J. Bacteriol.* **187,** 2233–2243 CrossRef Medline
34. Müller, P., Ewers, C., Bertsche, U., Anstett, M., Kallis, T., Breukink, E., Fraipont, C., Terrak, M., Nguyen-Distèche, M., and Vollmer, W. (2007) The essential cell division protein FtsN interacts with the murein (peptidoglycan) synthase PBP1B in *Escherichia coli*. *J. Biol. Chem.* **282,** 36394–36402 CrossRef Medline
35. Alexeeva, S., Gadella, T. W. J., Jr., Verheul, J., Verhoeven, G. S., and den Blaauwen, T. (2010) Direct interactions of early and late assembling division proteins in *Escherichia coli* cells resolved by FRET. *Mol. Microbiol.* **77,** 384–398 CrossRef Medline
36. Busiek, K. K., Eraso, J. M., Wang, Y., and Margolin, W. (2012) The early divisome protein FtsA interacts directly through its 1c subdomain with the cytoplasmic domain of the late divisome protein FtsN. *J. Bacteriol.* **194,** 1989–2000 CrossRef Medline
37. Massey, T. H., Mercogliano, C. P., Yates, J., Sherratt, D. J., and Löwe, J. (2006) Double-stranded DNA translocation: structure and mechanism of hexameric FtsK. *Mol. Cell.* **23,** 457–469 CrossRef Medline
38. LaPointe, L. M., Taylor, K. C., Subramaniam, S., Khadria, A., Rayment, I., and Senes, A. (2013) Structural organization of FtsB, a transmembrane protein of the bacterial divisome. *Biochemistry* **52,** 2574–2585 CrossRef Medline
39. van den Ent, F., Vinkenvleugel, T. M. F., Ind, A., West, P., Veprintsev, D., Nanninga, N., den Blaauwen, T., and Löwe, J. (2008) Structural and mutational analysis of the cell division protein FtsQ. *Mol. Microbiol.* **68,** 110–123 CrossRef Medline
40. Mosyak, L., Zhang, Y., Glasfeld, E., Haney, S., Stahl, M., Seehra, J., and Somers, W. S. (2000) The bacterial cell-division protein ZipA and its interaction with an FtsZ fragment revealed by X-ray crystallography. *EMBO J.* **19,** 3179–3191 CrossRef Medline
41. Tsang, M.-J., and Bernhardt, T. G. (2015) A role for the FtsQLB complex in cytokinetic ring activation revealed by an ftsL allele that accelerates division. *Mol. Microbiol.* **95,** 925–944 CrossRef Medline
42. Liu, B., Persons, L., Lee, L., and de Boer, P. A. J. (2015) Roles for both FtsA and the FtsBLQ subcomplex in FtsN-stimulated cell constriction in *Escherichia coli*. *Mol. Microbiol.* **95,** 945–970 CrossRef Medline
43. Khadria, A. S., and Senes, A. (2013) The transmembrane domains of the bacterial cell division proteins FtsB and FtsL form a stable high-order oligomer. *Biochemistry* **52,** 7542–7550 CrossRef Medline
44. Guzman, L. M., Weiss, D. S., and Beckwith, J. (1997) Domain-swapping analysis of FtsI, FtsL, and FtsQ, bitopic membrane proteins essential for cell division in *Escherichia coli*. *J. Bacteriol.* **179,** 5094–5103 CrossRef Medline
45. Gonzalez, M. D., and Beckwith, J. (2009) Divisome under construction: distinct domains of the small membrane protein FtsB are necessary for interaction with multiple cell division proteins. *J. Bacteriol.* **191,** 2815–2825 CrossRef Medline
46. Robichon, C., King, G. F., Goehring, N. W., and Beckwith, J. (2008) Artificial septal targeting of *Bacillus subtilis* cell division proteins in *Escherichia coli*: an interspecies approach to the study of protein-protein interactions in multiprotein complexes. *J. Bacteriol.* **190,** 6048–6059 CrossRef Medline

47. Gonzalez, M. D., Akbay, E. A., Boyd, D., and Beckwith, J. (2010) Multiple interaction domains in FtsL, a protein component of the widely conserved bacterial FtsLBQ cell division complex. *J. Bacteriol.* **192,** 2757–2768 CrossRef Medline
48. van den Berg van Saparoea, H. B., Glas, M., Vernooij, I. G. W. H., Bitter, W., den Blaauwen, T., and Luirink, J. (2013) Fine-mapping the contact sites of the *Escherichia coli* cell division proteins FtsB and FtsL on the FtsQ protein. *J. Biol. Chem.* **288,** 24340–24350 CrossRef Medline
49. Glas, M., van den Berg van Saparoea, H. B., McLaughlin, S. H., Roseboom, W., Liu, F., Koningstein, G. M., Fish, A., den Blaauwen, T., Heck, A. J. R., de Jong, L., Bitter, W., de Esch, I. J. P., and Luirink, J. (2015) The soluble periplasmic domains of *Escherichia coli* cell division proteins FtsQ/FtsB/FtsL form a trimeric complex with submicromolar affinity. *J. Biol. Chem.* **290,** 21498–21509 CrossRef Medline
50. Masson, S., Kern, T., Le Gouëllec, A., Giustini, C., Simorre, J.-P., Callow, P., Vernet, T., Gabel, F., and Zapun, A. (2009) Central domain of DivIB caps the C-terminal regions of the FtsL/DivIC coiled-coil rod. *J. Biol. Chem.* **284,** 27687–27700 CrossRef Medline
51. Noirclerc-Savoye, M., Le Gouëllec, A., Morlot, C., Dideberg, O., Vernet, T., and Zapun, A. (2005) *In vitro* reconstitution of a trimeric complex of DivIB, DivIC and FtsL, and their transient co-localization at the division site in *Streptococcus pneumoniae*. *Mol. Microbiol.* **55,** 413–424 Medline
52. Daniel, R. A., and Errington, J. (2000) Intrinsic instability of the essential cell division protein FtsL of *Bacillus subtilis* and a role for DivIB protein in FtsL turnover. *Mol. Microbiol.* **36,** 278–289 CrossRef Medline
53. Daniel, R. A., Noirot-Gros, M.-F., Noirot, P., and Errington, J. (2006) Multiple interactions between the transmembrane division proteins of *Bacillus subtilis* and the role of FtsL instability in divisome assembly. *J. Bacteriol.* **188,** 7396–7404 CrossRef Medline
54. Bramkamp, M., Weston, L., Daniel, R. A., and Errington, J. (2006) Regulated intramembrane proteolysis of FtsL protein and the control of cell division in *Bacillus subtilis*. *Mol. Microbiol.* **62,** 580–591 CrossRef Medline
55. Villanelo, F., Ordenes, A., Brunet, J., Lagos, R., and Monasterio, O. (2011) A model for the *Escherichia coli* FtsB/FtsL/FtsQ cell division complex. *BMC Struct. Biol.* **11,** 28 CrossRef Medline
56. Marks, D. S., Colwell, L. J., Sheridan, R., Hopf, T. A., Pagnani, A., Zecchina, R., and Sander, C. (2011) Protein 3D structure computed from evolutionary sequence variation. *PLoS One* **6,** e28766 CrossRef Medline
57. Hopf, T. A., Schärfe, C. P. I., Rodrigues JPGLM, Green, A. G., Kohlbacher, O., Sander, C., Bonvin, A. M. J. J., and Marks, D. S. (2014) Sequence coevolution gives 3D contacts and structures of protein complexes. *eLife* **3** CrossRef Medline
58. Ghigo, J.-M., and Beckwith, J. (2000) Cell division in *Escherichia coli*: role of FtsL domains in septal localization, function, and oligomerization. *J. Bacteriol.* **182,** 116–129 CrossRef Medline
59. McDonnell, A. V., Jiang, T., Keating, A. E., and Berger, B. (2006) Paircoil2: improved prediction of coiled coils from sequence. *Bioinformatics* **22,** 356–358 CrossRef Medline
60. Wolf, E., Kim, P. S., and Berger, B. (1997) MultiCoil: a program for predicting two- and three-stranded coiled coils. *Protein Sci.* **6,** 1179–1189 CrossRef Medline
61. Delorenzi, M., and Speed, T. (2002) An HMM model for coiled-coil domains and a comparison with PSSM-based predictions. *Bioinformatics* **18,** 617–625 CrossRef Medline
62. Lupas, A., Van Dyke, M., and Stock, J. (1991) Predicting coiled coils from protein sequences. *Science* **252,** 1162–1164 CrossRef Medline
63. Alva, V., Nam, S.-Z., Söding, J., and Lupas, A. N. (2016) The MPI bioinformatics Toolkit as an integrative platform for advanced protein sequence and structure analysis. *Nucleic Acids Res.* **44,** W410–W415 CrossRef Medline
64. Brown, J. H., Cohen, C., and Parry, D. A. (1996) Heptad breaks in α-helical coiled coils: stutters and stammers. *Proteins* **26,** 134–145 CrossRef Medline
65. Hicks, M. R., Walshaw, J., and Woolfson, D. N. (2002) Investigating the tolerance of coiled-coil peptides to nonheptad sequence inserts. *J. Struct. Biol.* **137,** 73–81 CrossRef Medline
66. Schmidt, N. W., Grigoryan, G., and DeGrado, W. F. (2017) The accommodation index measures the perturbation associated with insertions and deletions in coiled-coils: application to understand signaling in histidine kinases. *Protein Sci.* **26,** 414–435 CrossRef Medline
67. Strelkov, S. V., Schumacher, J., Burkhard, P., Aebi, U., and Herrmann, H. (2004) Crystal structure of the human lamin A coil 2B dimer: implications for the head-to-tail association of nuclear lamins. *J. Mol. Biol.* **343,** 1067–1080 CrossRef Medline
68. Adair, B. D., and Engelman, D. M. (1994) Glycophorin A helical transmembrane domains dimerize in phospholipid bilayers: a resonance energy transfer study. *Biochemistry* **33,** 5539–5544 CrossRef Medline
69. Levy, E. D., Pereira-Leal, J. B., Chothia, C., and Teichmann, S. A. (2006) 3D complex: a structural classification of protein complexes. *PLoS Comput. Biol.* **2,** e155 CrossRef Medline
70. Egan, A. J. F., and Vollmer, W. (2015) The stoichiometric divisome: a hypothesis. *Front. Microbiol.* **6,** 455 Medline
71. Harms, M. J., Schlessman, J. L., Sue, G. R., and García-Moreno, B. (2011) Arginine residues at internal positions in a protein are always charged. *Proc. Natl. Acad. Sci. U.S.A.* **108,** 18954–18959 CrossRef Medline
72. Mann, H. B., and Whitney, D. R. (1947) On a test of whether one of two random variables is stochastically larger than the other. *Ann. Math. Statist.* **18,** 50–60 CrossRef
73. Schymkowitz, J., Borg, J., Stricher, F., Nys, R., Rousseau, F., and Serrano, L. (2005) The FoldX web server: an online force field. *Nucleic Acids Res.* **33,** W382–W388 CrossRef Medline
74. Spearman, C. (1904) The proof and measurement of association between two things. *Am. J. Psychol.* **15,** 72–101 CrossRef
75. O'Leary, N. A., Wright, M. W., Brister, J. R., Ciufo, S., Haddad, D., McVeigh, R., Rajput, B., Robbertse, B., Smith-White, B., Ako-Adjei, D., Astashyn, A., Badretdin, A., Bao, Y., Blinkova, O., Brover, V., *et al.* (2016) Reference sequence (RefSeq) database at NCBI: current status, taxonomic expansion, and functional annotation. *Nucleic Acids Res.* **44,** D733–D745 CrossRef Medline
76. Li, W., Cowley, A., Uludag, M., Gur, T., McWilliam, H., Squizzato, S., Park, Y. M., Buso, N., and Lopez, R. (2015) The EMBL-EBI bioinformatics web and programmatic tools framework. *Nucleic Acids Res.* **43,** W580–W584 CrossRef Medline
77. Kamisetty, H., Ovchinnikov, S., and Baker, D. (2013) Assessing the utility of coevolution-based residue-residue contact predictions in a sequence- and structure-rich era. *Proc. Natl. Acad. Sci. U.S.A.* **110,** 15674–15679 CrossRef Medline
78. Kulp, D. W., Subramaniam, S., Donald, J. E., Hannigan, B. T., Mueller, B. K., Grigoryan, G., and Senes, A. (2012) Structural informatics, modeling, and design with an open-source Molecular Software Library (MSL). *J. Comput. Chem.* **33,** 1645–1661 CrossRef Medline
79. Subramaniam, S., and Senes, A. (2012) An energy-based conformer library for side chain optimization: improved prediction and adjustable sampling. *Proteins* **80,** 2218–2234 CrossRef Medline
80. Subramaniam, S., and Senes, A. (2014) Backbone dependency further improves side chain prediction efficiency in the Energy-Based Conformer Library (bEBL). *Proteins* **82,** 3177–3187 CrossRef Medline
81. MacKerell, A. D., Bashford, D., Bellott, M., Dunbrack, R. L., Evanseck, J. D., Field, M. J., Fischer, S., Gao, J., Guo, H., Ha, S., Joseph-McCarthy, D., Kuchnir, L., Kuczera, K., Lau, F. T. K., Mattos, C., *et al.* (1998) All-atom empirical potential for molecular modeling and dynamics studies of proteins. *J. Phys. Chem. B.* **102,** 3586–3616 CrossRef Medline
82. Krivov, G. G., Shapovalov, M. V., and Dunbrack, R. L. (2009) Improved prediction of protein side-chain conformations with SCWRL4. *Proteins* **77,** 778–795 CrossRef Medline
83. Ovchinnikov, S., Kinch, L., Park, H., Liao, Y., Pei, J., Kim, D. E., Kamisetty, H., Grishin, N. V., and Baker, D. (2015) Large-scale determination of previously unsolved protein structures using evolutionary information. *ELife* **4,** e09248 Medline
84. North, B., Summa, C. M., Ghirlanda, G., and DeGrado, W. F. (2001) D(n)-symmetrical tertiary templates for the design of tubular proteins. *J. Mol. Biol.* **311,** 1081–1090 CrossRef Medline
85. Brooks, B. R., Bruccoleri, R. E., Olafson, B. D., States, D. J., Swaminathan, S., and Karplus, M. (1983) CHARMM: a program for macromolecular energy, minimization, and dynamics calculations. *J. Comput. Chem.* **4,** 187–217 CrossRef

86. Kim, J.-K., Cho, Y., Lee, M., Laskowski, R. A., Ryu, S. E., Sugihara, K., and Kim, D.-S. (2015) BetaCavityWeb: a webserver for molecular voids and channels. *Nucleic Acids Res.* **43,** W413–W418 CrossRef Medline
87. Klauda, J. B., Venable, R. M., Freites, J. A., O'Connor, J. W., Tobias, D. J., Mondragon-Ramirez, C., Vorobyov, I., MacKerell, A. D., Jr., and Pastor, R. W. (2010) Update of the CHARMM all-atom additive force field for lipids: validation on six lipid types. *J. Phys. Chem. B* **114,** 7830–7843 CrossRef Medline
88. Phillips, J. C., Braun, R., Wang, W., Gumbart, J., Tajkhorshid, E., Villa, E., Chipot, C., Skeel, R. D., Kalé, L., and Schulten, K. (2005) Scalable molecular dynamics with NAMD. *J. Comput. Chem.* **26,** 1781–1802 CrossRef Medline
89. Jo, S., Kim, T., Iyer, V. G., and Im, W. (2008) CHARMM-GUI: a web-based graphical user interface for CHARMM. *J. Comput. Chem.* **29,** 1859–1865 CrossRef Medline
90. Humphrey, W., Dalke, A., and Schulten, K. (1996) VMD: visual molecular dynamics. *J. Mol. Graph.* **14,** 33–38, 27–28 CrossRef Medline
91. Laskowski, R. A., Rullmannn, J. A., MacArthur, M. W., Kaptein, R., and Thornton, J. M. (1996) AQUA and PROCHECK-NMR: programs for checking the quality of protein structures solved by NMR. *J. Biomol. NMR* **8,** 477–486 Medline
92. Studier, F. W. (2005) Protein production by auto-induction in high density shaking cultures. *Protein Expr. Purif.* **41,** 207–234 CrossRef Medline
93. Paintdakhi, A., Parry, B., Campos, M., Irnov, I., Elf, J., Surovtsev, I., and Jacobs-Wagner, C. (2016) Oufti: an integrated software package for high-accuracy, high-throughput quantitative microscopy analysis. *Mol. Microbiol.* **99,** 767–777 CrossRef Medline

The FtsLB subcomplex of the bacterial divisome is a tetramer with an uninterrupted FtsL helix linking the transmembrane and periplasmic regions

Samson G. F. Condon, Deena-Al Mahbuba, Claire R. Armstrong, Gladys Diaz-Vazquez, Samuel J. Craven, Loren M. LaPointe, Ambalika S. Khadria, Rahul Chadda, John A. Crooks, Nambirajan Rangarajan, Douglas B. Weibel, Aaron A. Hoskins, Janice L. Robertson, Qiang Cui and Alessandro Senes

J. Biol. Chem. 2018, 293:1623-1641.
doi: 10.1074/jbc.RA117.000426 originally published online December 12, 2017
